FERO: Finding extreme relativistic objects. I. Statistics of relativistic Fe Kα lines in radio-quiet Type 1 AGN

I. de La Calle Pérez, A. L. Longinotti, M. Guainazzi, S. Bianchi, M. Dovčiak, M. Cappi, G. Matt, G. Miniutti, P. O. Petrucci, E. Piconcelli, et al.

A&A 524, A50 (2010)
DOI: 10.1051/0004-6361/200913798

Astronomy & Astrophysics

FERO: Finding extreme relativistic objects

I. Statistics of relativistic Fe K_α lines in radio-quiet Type 1 AGN⋆

I. de la Calle Pérez[1], A. L. Longinotti[2,1], M. Guainazzi[1], S. Bianchi[3], M. Dovčiak[4], M. Cappi[11], G. Matt[3], G. Miniutti[5], P. O. Petrucci[6], E. Piconcelli[7], G. Ponti[8,9], D. Porquet[10], and M. Santos-Lleó[1]

[1] European Space Astronomy Centre of ESA, Apartado 50727, 28080 Madrid, Spain
e-mail: icalle@sciops.esa.int
[2] MIT Kavli Institute for Astrophysics and Space Research, Cambridge, USA
[3] Dipartimento di Fisica, Università degli Studi Roma Tre, via della Vasca Navale 84, 00146 Roma, Italy
[4] Astronomical Institute AS CR, Boční II 1401/1a, 14131 Praha 4, Czech Republic
[5] Centro de Astrobiología (CSIC-INTA); LAEFF, PO Box 78, Villanueva de la Cañada, Madrid 28691, Spain
[6] Laboratoire d'Astrophysique, UMR5571 Université J. Fourier/CNRS, Observatoire de Grenoble BP53, 38041 Grenoble Cedex 9, France
[7] Osservatorio Astronomico di Roma, via Frascati 33, 00040 Monteporzio Catone, Italy
[8] School of Physics and Astronomy, University of Southampton, Highfield, Southampton SO17 1BJ, UK
[9] APC, Université Paris 7 Denis Diderot, 75205 Paris, France
[10] Observatoire Astronomique de Strasbourg, Université Louis-Pasteur, CNRS, INSU, 11 rue de l'Université, 67000 Strasbourg, France
[11] INAF-IASF Bologna, via Gobetti 101, 40129 Bologna, Italy

Received 30 November 2009 / Accepted 27 July 2010

ABSTRACT

Context. Accretion models predict that fluorescence lines broadened by relativistic effects should arise from reflection of X-ray emission onto the inner region of the accretion disc surrounding the central black hole of active galactic nuclei (AGN). The theory behind the origin of relativistic lines is well established, and observational evidence from a moderate number of sources seems to support the existence of these lines.
Aims. The aim of this work is to establish the fraction of AGN with relativistic Fe K_α lines, and study possible correlations with source physical properties.
Methods. An XMM-Newton collection of 149 radio-quiet Type 1 AGN has been systematically and uniformly analysed in order to search for evidence of a relativistically broadened Fe K_α line. To enable statistical studies, an almost complete, flux-limited subsample of 31 sources has been defined by selecting the FERO sources observed by the RXTE all-sky Slew Survey with a count rate in the 3–8 keV energy band greater than 1 cts/sec. The 2–10 keV spectra of the FERO sources where compared with a complex model including most of the physical components observed in the X-ray spectra of Seyfert galaxies: a power law primary continuum modified by non-relativistic Compton reflection and warm absorption, plus a series of narrow Fe line reflection features.
Results. The observed fraction of sources in the flux-limited sample that show strong evidence of a relativistic Fe K_α line is 36%. This number can be interpreted as a lower limit to the fraction of sources that present a relativistic broad Fe K_α line in the wider AGN population. The average line equivalent width (*EW*) is of the order of 100 eV. The outcome of the fit yields an average disc inclination angle of 28 ± 5° and an average power-law index of the radial disc emissivity law of 2.4 ± 0.4. The spin value is well constrained only in 2 cases (MCG-6-30-15 and MRK 509); in the rest of the cases, whenever a constraint can be placed, it always implies the rejection of the static black hole solution. The Fe K_α line *EW* does not correlate with disc parameters or with system physical properties, such as black hole mass, accretion rate, and hard X-ray luminosity.

Key words. quasars: emission lines – galaxies: nuclei – galaxies: active – X-ray: galaxies

1. Introduction

The standard scenario for the X-ray emission in active galactic nuclei (AGN) assumes that the observed X-ray power-law continuum originates in the inner regions of the AGN closest to the central super-massive back hole, via inverse Compton scattering of soft-energy photons in a corona of relativistic electrons located somewhere above the accretion disc (e.g. Haardt & Maraschi 1993). The X-ray illumination of optically thick cold matter, such as the molecular torus and/or the accretion disc, gives rise to a Compton reflection spectral component containing a series of fluorescent lines from K_α transitions in metal atoms (e.g. George & Fabian 1991). From a combination of fluorescence yield (proportional to the fourth power of the atomic number) and cosmic abundance, the most prominent is the K_α line emitted by neutral iron at 6.4 keV.

When the Compton reflection originates in distant material like the molecular torus envisaged in unification models (Antonucci 1993), the profile of the Fe K_α emission line is narrow and unresolved by present X-ray detectors. In contrast, the reflection component originating in the inner accretion disc is affected by the black hole's strong gravitational field, which modifies the line profile. The numerous studies of the effect of gravity on the narrow emission line all agree by describing the resulting

⋆ Appendices are only available in electronic form at http://www.aanda.org

relativistic profile as skewed and asymmetric because of a combination of kinematic and relativistic effects (e.g. Fabian et al. 2000), with a red wing extending towards low X-ray energies due to gravitational redshift and transverse Doppler redshift (e.g. Fabian et al. 1989).

Since relativistic lines originate within a few gravitational radii from the central object, the study of their shape and intensity may represent a potential probe of the physical processes taking place in the innermost regions of the AGN. The line profile is in fact very sensitive to the accretion disc properties, such as the radial extension and dependence of the line emissivity, the ionisation state of the material, the observer's inclination angle relative to the disc axis, and the spin of the black hole (for a review see Reynolds & Nowak 2003; Fabian & Miniutti 2009; Matt 2006, and references therein).

The first unambiguous observational evidence of relativistic Fe K_α lines in the X-ray spectra of AGN was found in the spectrum of MCG-6-30-15 obtained by the *ASCA* satellite (Tanaka et al. 1995) and lately, in several other Seyfert Galaxies (Nandra et al. 1997) to the point where the broad line was considered a common feature of AGN. Nevertheless, the presence of relativistic broad Fe K_α lines is nowadays more controversial than ever since only a handful of sources seem to possess a truly relativistically broadened Fe K_α line, e.g. MCG-6-30-15 (Fabian et al. 2002) or NGC 3516 (Markowitz et al. 2008). When studies based on sizable samples of sources are considered, the average fraction of sources with relativistic broad Fe K_α lines is never higher than 40% (Porquet et al. 2004; Jiménez-Bailón et al. 2005; Guainazzi et al. 2006; Nandra et al. 2007).

In the past decade the advent of *Chandra*, *XMM-Newton* and *Suzaku* has undoubtedly provided deeper knowledge and more thorough understanding of AGN X-ray spectral properties by means of superior spectral resolution and higher throughput. For instance, it has been confirmed that about half of quasars and Seyfert galaxies show the so-called warm absorbers, i.e., ionised material outflowing along the line of sight, which is revealed as a series of absorption features imprinted mainly in the soft X-ray spectral band (Piconcelli et al. 2005; Blustin et al. 2005, and references therein). Emission lines from highly ionised atoms, including iron, can also be observed (see Bianchi et al. 2005). The presence of this absorbing/emitting gas may introduce further complexities into the Fe K band: it has been shown that warm absorbers with sufficiently high column density and ionisation state may distort the continuum underlying the iron line, mimicking a relativistic broad red wing (e.g. NGC 3783, Reeves et al. 2004, and MCG-6-30-15, Miller et al. 2008; see also Turner & Miller 2009 for a review). Also, a blend of emission lines from helium and hydrogen-like iron at 6.7–6.97 keV can be mistaken for a broad disk line observed at high inclination (NGC 7314, Yaqoob et al. 2003, and MRK 590, Longinotti et al. 2007). While the latter scenario is fully taken into account in our baseline model, only a simple parameterization of the warm absorber was adopted, because an unknown number of a priori absorbing systems do not allow a systematic analysis to be performed (see Sect. 3.3 for details).

The FERO (finding extreme relativistic objects) project is part of a wider investigation on AGN carried out on archival *XMM-Newton* data (see Sect. 2). It was designed to address two fundamental questions on the relativistic broad Fe K_α line:

i) how common is relativistic broadening in AGN, and
ii) does the presence of a broad line depend on other source's physical properties ?

To try to answer these questions, all the sources in our sample were fitted with one and the same model, which includes all absorption and emission components known to be potentially present in AGN (see Sect. 3.3) and able to affect the emission in the iron K band.

This paper reports the results of the spectral analysis on the individual sources of the sample. A companion paper (Longinotti et al., in prep.) is devoted to the analysis of stacked spectra. The structure of this paper is as follows. Section 2 describes the selection of the sample. Section 3 describes the analysis procedure, including the spectral analysis and the spectral model used to describe our data. Section 4 summarizes our results to be discussed in Sect. 5. Section 6 closes the paper with the conclusions drawn from the study presented here.

2. The sample

The FERO AGN collection proceeds from the CAIXA catalogue of AGN recently published by Bianchi et al. (2009a,b). CAIXA is the largest catalogue of high signal-to-noise X-ray spectra of AGN which consists of all the radio-quiet X-ray unobscured ($N_{\rm H} < 2\times10^{22}{\rm cm}^{-2}$) AGN observed by *XMM-Newton* in targeted observations, whose data are public as of March 2007. The sample, through a complete and homogeneous spectral analysis, is characterized in terms of the parameters adopted by the best-fit models. CAIXA includes a total of 77 quasars and 79 Seyfert galaxies. The redshift distribution spans from $z = 0.002$ to $z = 4.520$ (almost 90% within $z < 1$) and the distribution of the hard X-ray luminosities covers a range between $L_{2-10\ {\rm keV}} = 2.0\times10^{41}-3.9\times10^{46}$ erg s^{-1}. Since the source selection criteria used in this work are by large the same described there, the reader is deferred to these works for more details. Here, those general aspects that are more relevant to the relativistic line analysis carried out in this work are recalled.

2.1. The FERO AGN collection

The starting sample consisted of 161 radio-quiet X-ray unobscured sources targeted by *XMM-Newton* with public data up to April 2008. Only sources with local column density from cold gas lower than $N_{\rm H} \leq 2\times10^{22}$ cm^{-2} are included in the sample to avoid heavily absorbed spectra in the 2 to 10 keV spectral region. With respect to CAIXA (which sums up 156 sources), the following 5 AGNs were added: ESO 511-G030, IRAS 05078+1626, MRK 704, NGC 3227, NGC 526A. The first three sources were specifically proposed and granted in the *XMM-Newton* AO6 for the purpose of the FERO project; the other two objects became publicly available in the data archive during the development of the FERO analysis. NGC 4151 fullfills the required conditions to be in our sample, but it was excluded (both from FERO and CAIXA) based on its complex X-ray spectra and extreme spectral variability attributed to several absorbing systems (Puccetti et al. 2007). Based on a signal-to-noise criterion, as reasoned in Sect. 3.2, 12 sources are dropped from the starting sample, leaving what constitutes the FERO sample with a total of 149 sources.

Out of the 149 sources, 67 are classified as quasars (RQQs) and 82 classified as Seyfert 1s (Sy) according to the value of the absolute optical magnitude $M_{\rm B}$ (QSO $M_{\rm B} < -23$; Sy $M_{\rm B} > -23$) as defined in the Véron-Cetty and Véron catalogue 2006 (Véron-Cetty & Véron 2006). Radio Loud objects are excluded from the sample according to the value of the radio-loudness parameter (R; Stocke et al. 1992). For QSO the condition $\log(R) > 1$ is applied to reject a source, while in the case of Seyferts, in addition

to $\log(R) > 2.4$, sources are also excluded if $\log(R_X) > -2.755$ (Panessa et al. 2007), where R_X is the X-ray radio-loudness parameter (Terashima & Wilson 2003) (see Bianchi et al. 2009a for details). No redshift restriction has been imposed in our sample, which contains mostly local sources with 90% of the sources at a redshift $\leq$0.5 and 60% at a redshift $\leq$0.1. A distinction has been made between Broad Line (BL; 40% of full sample) and Narrow Line (NL; 20% of full sample) sources, using as threshold the value of the Full Width Half Maximum (*FWHM*) of the H_β line whenever available (65% of the sources in our sample): $H_\beta \geq 2000$ km s^{-1} for BL and $H_\beta < 2000$ km s^{-1} for NL (Osterbrock & Pogge 1987). This distinction between NL and BL refers only to this standard limit on H_β, while no optical Type 2 objects are present in the sample. When needed, and not derived in this work, source properties are extracted from the CAIXA catalogue.

2.2. The Flux-limited sample

The selection criteria with which CAIXA and FERO were assembled do not provide a complete sample in the sense that the sources are not selected according to a physical property: the main point of the FERO project is to include as many objects as possible and this of course depends predominantly on the availability of public observations. Because of the nature of the FERO project, one of the fundamental requirements was to identify a complete, unbiased subsample of sources with high signal to noise in order to derive meaningful constraints on the properties of the (unknown) parent population of local radio-quiet AGN. Hence, sources from the RXTE all-sky Slew Survey (XSS, Revnivtsev et al. 2004) having a count rate in the 3–8 keV energy band greater than 1 cts/sec and fulfilling the FERO source selection criteria were identified. This defines a flux-limited sample of 33 sources. The XSS is nearly 80% complete at the selected flux level for sources with Galactic latitude greater than 10°. For two of them, UGC 10683 and ESO 0141-G055, no *XMM-Newton* data were available as of April 2008. This leaves the number of XSS-selected bright sources in the FERO sample to 31 (listed in Table A.1 in Appendix A). Throughout the paper, these 31 sources will be referred to as the flux-limited sample.

3. Analysis

The data corresponding to the 149 observations have been uniformly analysed using SASv6.5 (Gabriel et al. 2004) and the latest calibration files available. Event lists were obtained for the EPIC-pn camera following standard SAS data reduction procedures. Due to its larger effective area, only EPIC-pn (Strüder et al. 2001) data has been considered in this work. The filtering of event lists for periods of high background activity was performed by maximizing the source signal to noise as in Piconcelli et al. (2004). The typical source extraction regions are circular and of the order of 50″in radii for small window mode, while for full frame and large window modes, the source extraction regions range from 20 to 40″in radii. Background spectra were extracted from circular source-free regions, except for observations taken in small window mode where blank-field event lists were used as described in Read & Ponman (2003), of a 50″in radii and close to the target. Spectra affected by a pileup larger than 1% were rejected. Full details of the data reduction and spectra accumulation are reported in Bianchi et al. (2009a).

3.1. XMM-Newton observations

The data of the observations presented here were public as of April 2008. All the observations are target observations with exposure times ranging between 1 ks and 400 ks, with 90% of the observations below 100 ks.

3.1.1. Multiple observations

When multiple observations of the same source were available, the individual spectra were combined and treated, for all purposes, as a single observation. The FTOOLS tasks *mathpha*, *adrmf*, and *addarf* were used correspondingly to sum the source and background counts spectra and the response matrix and ancillary files, using the exposure times of the individual observations to be summed as weights in these last two cases. However, spectra were only combined if the observations were taken with the same observing mode and if the source was in *similar* flux state, i.e., if the total flux and power-law spectral index in the 2–10 keV energy band were consistent within the statistical errors. If these criteria were not met, then the observation with the longest exposure time was chosen to prevent introducing source-related bias in the selection. This procedure ensures that mixing different observations from a given source does not affect the results derived from our data set.

A total of 22 sources in our sample have multiple observations. Table 1 lists on a source-by-source basis *XMM-Newton* observation IDs that have been combined. For completeness, Table B.1 in Appendix B lists those sources for which multiple observations are available, but only one was considered; so no spectra were combined. This approach is different from the one taken in CAIXA, where for sources with multiple observations, the one with the longest exposure was selected systematically as independent of the flux state. The importance of achieving high signal-to-noise spectra for the FERO project, meant that it was preferred to co-add multiple observations of the same source, when available.

3.2. Spectral analysis

The time-averaged spectra were re-binned in order not to oversample the intrinsic energy resolution of the EPIC-pn camera ($\simeq$150 eV at 6 keV) by a factor larger than 3, while making sure that each spectral channel contains at least 25 background-subtracted counts to ensure the applicability of the χ^2 goodness-of-fit test. Fits were performed in the 2–10 keV energy range. To ensure good quality spectral fits, only those source spectra with at least 17 d.o.f. in this energy range were considered in the analysis. (12 out of the 161 sources in the initial sample did not meet this criterion.) For the spectral analysis and fitting, XSPEC v12.3.0 (Arnaud 1996) was used. Throughout the analysis, solar abundances were assumed after Anders & Ebihara (1982).

3.3. Spectral model

All spectra were fitted with the following baseline model:

$$e^{-\sigma N_{\rm H}} \cdot W(\Gamma, N_{\rm H}^i, \xi) \cdot A[E^{-\Gamma} + C(\Gamma, R) + \sum_{i=1}^{5} G_i + Ky(\theta, \beta, a)] \quad (1)$$

where the different model components are

- Galactic absorption ($e^{-\sigma N_{\rm H}}$), where $N_{\rm H}$ was fixed to the galactic column density and σ is the photoelectric cross section of the process according to Morrison & McCammon (1983);
- Power law ($N(E) \propto E^{-\Gamma}$), where Γ is the photon index of the primary power-law X-ray source spectrum;

Table 1. List of sources within the FERO sample where multiple observations are available.

Source name	List of *XMM-Newton* observation IDs combined	Observation date	Observation exposure time (ks)	Source name	List of *XMM-Newton* observation IDs combined	Observation date	Observation exposure time (ks)
PG 1440+356	**0005010101**	2003-01-01	17.2	1H0419-577	**0148000401**	2003-03-30	11.1
	0005010201	2003-01-04	10.6		**0148000501**	2003-06-25	10.7
	0005010301	2003-01-07	18.1		**0148000601**	2003-09-16	11.3
	0107660201	2001-12-23	24.2		0148000201	2002-09-25	11.8
AKN 564	**0006810101**	2000-06-17	7.4		0148000301	2002-12-27	7.6
	0006810301	2001-06-09	7.5		0148000701	2003-11-15	1.1
	0206400101	2005-01-05	69.2		0112600401	2000-12-04	5.7
MCG-6-30-15	**0029740101**	2001-07-31	55.8	PG1115+080	**0203560201**	2004-06-10	65.5
	0029740701	2001-08-02	85.7		**0203560401**	2004-06-26	71.2
	0029740801	2001-08-04	86.8		**0082340101**	2001-11-25	53.8
	0111570101	2000-07-11	28.8	IRAS17020+4544	**0206860101**	2004-08-30	13.4
	0111570201	2000-07-11	37.9		**0206860201**	2004-09-05	12.3
NGC 5548	**0089960301**	2001-07-09	58.7	MRK 507	**0300910401**	2005-06-17	15.8
	0109960101	2000-12-24	16.0		**0300910701**	2005-09-01	11.4
	0089960401	2001-07-12	19.8	MRK 279	**0302480401**	2005-11-15	41.4
MRK 876	**0102040601**	2001-04-13	2.6		**0302480501**	2005-11-17	40.7
	0102041301	2001-08-29	2.4		**0302480601**	2005-11-19	22.8
ESO15-IG011	**0103861701**	2000-09-29	5.0	MRK 766	**0109141301**	2001-05-20	89.6
	0103862001	2001-10-31	4.5		**0304030301**	2005-05-25	68.9
MCG-01-13-025	**0103863001**	2002-08-28	4.3		**0304030401**	2005-05-27	65.8
	0103861401	2000-08-30	1.5		**0304030501**	2005-05-29	64.9
NGC 3516	**0107460601**	2001-04-10	64.3		**0304030601**	2005-05-31	63.1
	0107460701	2001-11-09	88.7		**0304030701**	2005-06-03	20.4
REJ2248-511	**0109070401**	2000-10-26	10.1		0096020101	2000-05-20	25.7
	0109070601	2001-10-31	9.8		0304030101	2005-05-23	66.2
H0557-385	**0109130501**	2002-04-03	4.0	SDSSJ135724.51+652505.9	**0305920301**	2005-04-04	21.1
	0109131001	2002-09-17	6.5		**0305920601**	2005-06-23	12.0
TONS 180	**0110890401**	2000-12-14	20.3	LBQS1228+1116	**0306630101**	2005-12-13	60.4
	0110890701	2002-06-30	12.6		**0306630201**	2005-12-17	83.2
NGC 7469	**0112170101**	2000-12-26	12.3	MRK 509	**0306090201**	2005-10-18	59.8
	0112170301	2000-12-26	16.1		**0306090301**	2005-10-20	32.4
	0207090101	2004-11-30	59.2		**0306090401**	2006-04-25	48.6
	0207090201	2004-12-03	55.0		**0130720201**	2001-04-20	27.8
NGC 3783	**0112210101**	2000-12-28	26.1		0130720101	2000-10-25	20.7
	0112210201	2001-12-17	51.2				
	0112210501	2001-12-19	93.2				

Notes. Multiple observations were combined where available and treated, for all purposes, as a single observation. Observation IDs in bold correspond to those observations that were combined, while observation IDs not marked in bold were discarded.

- Compton reflection from neutral material ($C(\Gamma, R)$), where R is the reflection factor as compared to material emitting over 2π in solid angle (see however Murphy & Yaqoob 2009 for some *caveats* about this interpretation). The high-energy cut-off of the primary spectrum was fixed to 100 keV. The viewing angle of the reflecting material was fixed to 18°, while the reflection normalization (R) was left free during the fitting procedure. The model used was the XSPEC PEXRAV component (Magdziarz & Zdziarski 1995);
- Ionised absorption ($W(\Gamma, N_{\rm H}^{i}, \xi)$) from warm gas in the local AGN environment was introduced through the XSPEC model ABSORI. Although more accurate and complex models exist for warm absorption, they would overfit the lower-quality data in our sample when uniformly applied to the whole sample. Both the intrinsic column density ($N_{\rm H}^{i}$) and ionisation parameter (ξ) were left free during the fitting procedure, while the continuum slope (Γ) was tied to the photon index of the primary power-law continuum. The temperature of the absorber was fixed to 2×10^5 K (~17 eV), representative of the temperature found in warm absorbers (see e.g. Krongold et al. 2007);
- Narrow lines (G_i): 4 zero-width Gaussian lines were included with centroid energies fixed at 6.4 keV (neutral Fe I K_α), 6.7 keV (ionised Fe XXV), 6.96 keV (ionised Fe XXVI), and 7.06 keV (neutral Fe I K_β). The normalization of the Fe I K_β line was limited to less than 16% that of the Fe I K_α line flux (Molendi et al. 2003). The two ionised lines were included in the baseline model as several studies show that they represent an important spectral component in AGN. Among the possible physical interpretations of these features are an origin in the accretion disc (e.g. Reeves et al. 2001; Pounds et al. 2001; Miller et al. 2007) or produced in photoionised circumnuclear matter (e.g. Bianchi & Matt 2002; Bianchi et al. 2005);
- Fe I 6.4 keV Compton shoulder (G_i). The Fe I K_α Compton shoulder of the narrow component of the Fe I fluorescent line was considered by using a Gaussian line at 6.3 keV, with 0.05 keV as the fixed width and free normalization allowed

to be no more than ~20% that of the 6.4 keV Fe I K$_\alpha$ line, following Matt (2002);

- Relativistic line ($Ky(\theta, \beta, a)$, *Kyrline* model). To model the effect of the strong gravitational field on the emission regions of the disc closest to the central black hole, the *Ky* set of models within XSPEC was used (Dovčiak et al. 2004). The model considers accretion disc emission around a rotating black hole with a given spin, a. In contrast to models such as *diskline* or *laor*, *Kyrline* allows the spin to be fitted as a free parameter. For the line emission, a fixed centroid energy of 6.4 keV (in the rest frame of the source), is assumed, while the emission between the innermost stable orbit and 400 gravitational radii is integrated, keeping these limits fixed during the fitting procedure. The radial dependence of the disc emission is modelled with a power law of index β ($\propto r^{-\beta}$), while Laor's limb darkening law was adopted to characterize the angular dependence. Here, the radial disc emissivity is referred to as β. The disc inclination angle (θ), β, and a are free parameters during the fitting procedure.

In summary, the model that was uniformly fitted to our data consists of 9 components with a total of 14 free independently-fitted parameters. For those cases in which the value of the *FWHM* of the H$_\beta$ line is available, the model has 15 free parameters (see Sect. 3.3.1). The fitting procedure was carried out over different steps. First, the power law with neutral reflection and absorption were fitted to the data, followed by the addition of the narrow line components one by one (in the order listed above). The last model component added to the fit was the relativistic line. After each addition of a new component, a fit was performed, and no model component discarded regardless of the goodness-of-fit. This implies that the χ^2 values obtained from the fits correspond to the best-fit given by this model. Its important to stress that no attempt has been made as a whole or on a source-by-source basis to find the best-fit model yielding the lowest possible χ^2 value. For reference, Table C.1 gives, for those sources belonging to the flux-limited sample, the most relevant parameters of the best fit for the model considered.

3.3.1. Limitations to model parameters

During the fitting procedure, some limitations are introduced for the following parameters of the baseline model:

- The disc inclination angle in the *Kyrline* model was limited to a maximum value of 60°. In the Seyfert unification scenario (Antonucci 1993), Type 1 objects are not expected to have large viewing angles. It has been found that relaxing the restriction on the inclination angle yields a number of detections of broad and highly skewed lines with equivalent widths of the order of 1 keV. This effect is simply because in sources with poor statistics above 7 keV, the broad line model fits the continuum, also reflected by required large disc-inclination angles (>80°).
- The disc emissivity in the *Kyrline* model was limited to a maximum value of 6 given that steeper profiles are not expected, even taking strong general relativistic effects into account on the primary emission such as light bending (see Miniutti & Fabian 2004).
- To possibly constrain the parameter space, limitations to the spin parameter in the *Kyrline* model were tested. Three fitting runs were produced with black hole spin fixed to 0.998 (*Kerr*), fixed to 0 (*Schwarzschild*), and free to vary between 0 and 0.998. In the first two cases, no systematic difference was found when comparing the results in terms of χ^2 improvement, leading us to conclude that none of the two extreme spin values can be assumed a priori. Therefore, the results presented are extracted from the run where the black hole spin is left free to vary during the fitting procedure.
- The power-law index (Γ) and the reflection fraction (R) were limited following the work by Dadina (2008) on a *BeppoSAX* sample of Type 1 Seyfert galaxies. Given the distributions of Γ and R derived by Dadina (2008), a limit of three times the 1σ standard deviation of the average values is chosen for Γ and R ($\Gamma \in [0.45{:}3.33]$; $R \in [0.{:}3.33]$).
- When available in the literature, the value of the *FWHM* of the optical H$_\beta$ line was used to set an upper limit to the width of the narrow component of the 6.4 keV neutral Fe I K$_\alpha$ line, leaving the width of the line free. This choice is consistent with the possibility that for some sources, the Fe I K$_\alpha$ line may be produced in the optical broad line region (see e.g. Bianchi et al. 2008 and references therein). When the H$_\beta$ *FWHM* was not available, the Fe I K$_\alpha$ line width was assumed to be unresolved ($\sigma \equiv 0$).

3.3.2. Test of spectral model components

During the process of selecting the baseline model, several tests were performed with different model components. The most important ones are summarised below.

- To contemplate the hypothesis that the reprocessed AGN continuum in Type 1 objects is made by contribution of both torus and disc reflection, the presence of two reflection components at the same time was tested. The second PEXRAV disc component was relativistically blurred using the convolution model *kdblur*, to take possible relativistic effects into account. After close inspection of the contribution from each physical system, it was concluded that the sensitivity band of *XMM-Newton* does not allow disentangling the reflection component from the torus from that of the disc. Since the presence of torus reflection is very well supported observationally by the almost ubiquitous narrow Fe I K$_\alpha$ component (Bianchi et al. 2004; Yaqoob & Padmanabhan 2004), only this PEXRAV component has been included in our baseline model.
- The effect of reflection from an ionised accretion disc was tested by replacing the torus reflection with the model component PEXRIV (Magdziarz & Zdziarski 1995): Eq. (1) is thus modified to include the disc ionisation parameter ξ in the function C(Γ, R), which is left free during the fitting procedure. The centroid energy in the *Kyrline* model was consistently set to 6.7 keV. The results from this test are discussed in Sects. 4 and 5.

4. Results

The *EW* of the *Kyrline* component was used as a proxy for establishing significant detections of relativistic Fe I K$_\alpha$ lines in the sample. The line *EW* is defined in this work as the ratio of the flux of the *Kyrline* component to the flux of the continuum, as defined in Sect. 3.3, integrated over the energy range between ±5% around the line rest-frame energy (6.4 keV). The error in the normalization of the *Kyrline* component is used to estimate the uncertainty in the corresponding line *EW*. The threshold for significant detections is set to 5σ confidence level (c.l.). This is a somewhat more conservative approach than normally taken when reporting relativistic line detections in individual objects,

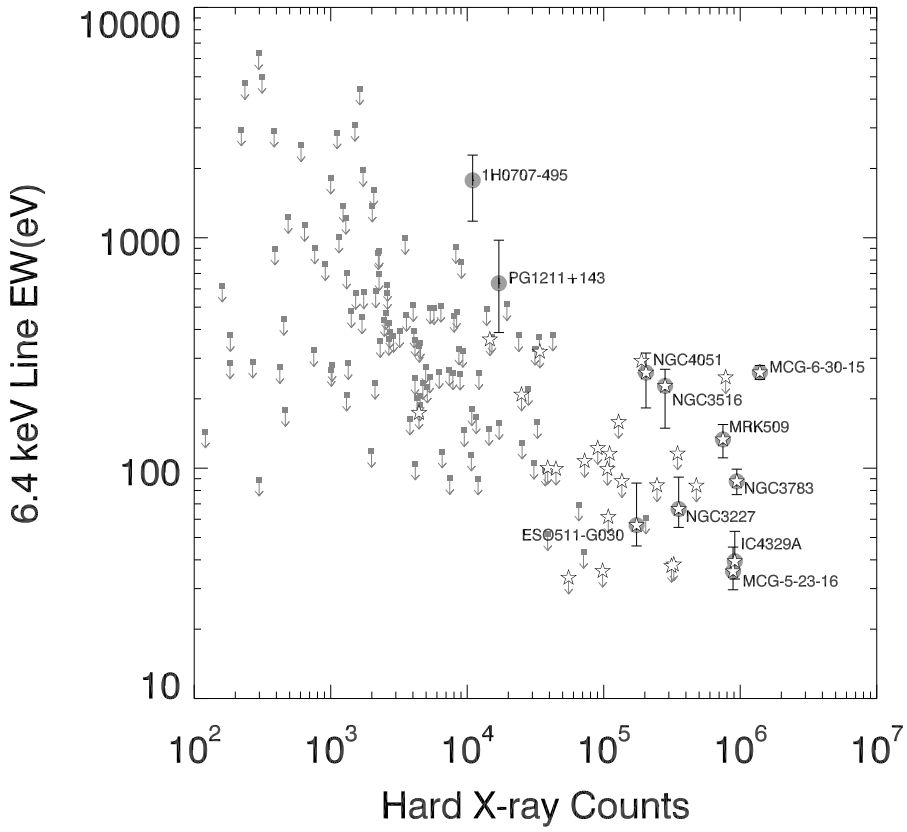

Fig. 1. Equivalent width of the relativistic broad 6.4 keV Fe K_α line vs. hard X-ray counts (2–10 keV) for the FERO sources. Filled circles indicate line detections at $\geq 5\sigma$ confidence level (where error bars indicate the 90% confidence level intervals), while filled squares indicate line upper limits at the 90% confidence level. White stars indicate sources belonging to the flux-limited sample (see Sect. 2.2, for details).

but it has to be kept in mind that the FERO project is a statistical study of a large sample that includes spectra of very different levels of statistical quality. For those sources with no significant line detection, the upper limits to the line *EW* at the 90% c.l. are provided. In the following, errors, upper and lower limits, on the relevant parameters are given at the 90% c.l. for one interesting parameter ($\Delta\chi^2 = 2.71$).

4.1. Sources with detected broad Fe lines.

Figure 1 shows the *EW* of the broad Fe K_α line at 6.4 keV as a function of source counts in the 2–10 keV band. This plot shows two things. First, significant broad Fe K_α line detections are concentrated in the portion of the plot dominated by spectra with good statistical quality (roughly with $\gtrsim 1.5\times10^5$ hard X-ray counts). Second, overall, the distribution of line *EW* upper limits versus hard X-ray counts follows the expected trend; i.e., in the absence of a significant broad line, the sensitivity (the ability to detect a broad line) goes as $(1/\sqrt{(cts_{2-10\ \mathrm{keV}})}$. The dispersion of *EW* upper limits around this direction, for a given range of hard X-ray counts, could be explained in terms of scattering of the model parameters.

Table 2 provides the detailed list of the significant relativistic broad Fe K_α line detections with the best-fit parameters of the *Kyrline* model. From now on, this table is referred to as the list of detected relativistic Fe K_α lines in the FERO sample. In the fitting procedure, relativistic effects from neutral and ionised reflection were tested as explained in Sect. 3.3.2. The test for a neutral Fe K_α broad line yields in total 11 significant detections at $\geq 5\sigma$ c.l.. The fit with the model with an ionised Fe K_α line yields a detection in all the 11 sources, except IC4329A, 1H0707-495, and MCG-5-23-16, which only provide detection in the neutral case. In the 8 sources where a relativistic broad Fe K_α line is equally detected by means of neutral and ionised reflection models, the best-fit models were carefully examined and the model with the lowest χ^2 preferred. MRK 509 is the only source for which the ionised reflection provides a significant better-fit statistic (with the probability of the improvement being by chance of 2.2×10^{-7}). MRK 766 and ARK 120 on the contrary, show significant broad Fe lines only in the ionised case. At the end, neutral and ionised runs were merged, which yields 13 sources with strong evidence of a broad Fe line. Last, it is worth pointing out that the only source where a relativistic broad Fe K_α line is claimed for the first time in this work is ESO511-G030, with an *EW* of 57^{+30}_{-11} eV.

Two sources, PG1211+143 and 1H0707-495, are characterised by extremely high *EW* of the Fe K_α line (Figure 1, see also Table 2). The data included in our sample for both sources have similar spectral shapes, showing deep spectral features at ~7 keV and spectral curvature in the Fe energy band. Pounds et al. (2003a) argue that PG1211+143 presents a high column density (5×10^{23} cm^{-2}) of highly ionised matter along the line of sight partially covering the central hard X-ray source and that the apparent presence of a relativistic Fe K_α emission line could be an artifact of absorption. However, the relativistic broad line interpretation is not discarded, and the same authors find that a broad line with a large *EW*, of the order of 600–900 eV, and a combination of absorption features, provide a good interpretation of the data. This value of the Fe K_α line *EW* is in good agreement with the value found in this work (635^{+341}_{-247} eV). Nevertheless, whether there is a relativistically broadened Fe K_α line in this source is debatable, as new results from a more recent analysis on data from 2007 indicate (Pounds et al. 2009). 1H0707-495 also shows a prominent flux drop around 7 keV, which can be modelled with an absorption edge assuming large Fe overabundance (Gallo et al. 2004). Fabian et al. (2004) interpret the drop around 7 keV in terms of relativistically blurred ionised reflection from the accretion disc, and derive an *EW* for

Table 2. Sources within the FERO sample where a relativistic Fe K_α line is detected with a significance $\geq 5\sigma$.

Source	Type[(1)]	$L_X^{2-10\ keV}$ (10^{42} erg s^{-1})	$Cts^{2-10\ keV}$ (10^5 cts)	*EW* (eV)	θ (°)	a	β	χ^2/d.o.f.	References[(2)]
IC 4329A	BLSY	56.4	9.123 ± 0.009	39^{+14}_{-6}	28^{+6}_{-11}	≥0.0	<1.3	238.1/161	**(1)**, **(2)**, (3), (4)
MCG-5-23-16	NCSY	14.2	8.853 ± 0.009	36^{+10}_{-6}	21^{+8}_{-3}	≥0.0	<1.6	271.4/162	**(5)**, **(6)**
ESO511-G030	NCSY	22.4	1.740 ± 0.004	57^{+30}_{-11}	18^{+7}_{-7}	≥0.0	<1.1	198.2/161	
MCG-6-30-15	BLSY	5.4	13.927 ± 0.012	260^{+19}_{-18}	40^{+1}_{-3}	$0.86^{+0.01}_{-0.02}$	$4.1^{+0.2}_{-0.2}$	227.6/161	**(7)**, **(8)**, **(9)**, (10)
NGC 4051	NLSY	0.3	2.040 ± 0.004	260^{+56}_{-77}	22^{+6}_{-6}	>0.46	$2.9^{+0.3}_{-0.4}$	198.8/162	**(11)**, **(12)**, (13)
NGC 3516	BLSY	3.6	2.810 ± 0.005	227^{+41}_{-78}	27^{+2}_{-3}	>0.48	$2.8^{+0.2}_{-0.3}$	223.1/161	**(14)**, **(15)**, (16)
NGC 3783	BLSY	11.4	9.440 ± 0.010	88^{+11}_{-11}	<8	>0.16	$2.7^{+0.1}_{-0.2}$	304.5/161	**(17)**, (18)
NGC 3227	BLSY	1.2	3.541 ± 0.006	66^{+25}_{-11}	23^{+4}_{-4}	≥0.0	$1.9^{+0.6}_{-0.5}$	230.9/162	**(19)**, (20)
MRK 509 (*)	BLQ	103.5	7.471 ± 0.009	170^{+26}_{-19}	53^{+1}_{-1}	$0.78^{+0.03}_{-0.04}$	>3.8	277.3/158	**(21)**, **(22)**
MRK 766 (*)	NLSY	6.1	7.816 ± 0.008	234^{+23}_{-49}	20^{+3}_{-2}	>0.47	$2.7^{+0.2}_{-0.1}$	300.3/160	**(23)**, (24)
ARK 120 (*)	BLSY	90.5	3.473 ± 0.006	140^{+31}_{-41}	>59	≥0.0	$2.2^{+0.6}_{-0.3}$	212.3/158	**(25)**
1H0707-495	NLSY	46.8	0.110 ± 0.001	1775^{+511}_{-594}	54^{+3}_{-3}	≥0.93	$4.13^{+1.22}_{-0.65}$	107.6/116	**(26)**, **(27)**, (28)
PG 1211+143	NLQ	49.4	0.171 ± 0.001	635^{+341}_{-247}	52^{+4}_{-7}	≥0.92	>4.37	160.7/139	**(29)**, (30)

Notes. (*) 6.7 keV K_α line is preferred; * Sources for which there is a significant detection of a relativistic *ionised 6.7* keV K_α *line* (see text for details). The first 11 sources listed in the table belong to the flux-limited sample. θ, a, and β are the disc inclination angle with respect to the observer, the black hole spin and disc emissivity, respectively, of the best-fit parameters of the *Kyrline* model. Except for the hard X-ray counts where 1σ errors are given, errors in any given parameter are given at the 90% confidence level. Also, upper and lower limits in any relevant paremeter are given at the 90% confidence level.
[(1)] SY: Seyfert, Q: quasar, NL: narrow line, BL: broad line, NC: not classified. [(2)] References where evidence for a relativistic Fe K_α line for a particular object is reported (references marked in bold) as well as those where alternative scenarios are provided. The list of references is not meant to be complete.

References. (1) Done et al. (2000); (2) McKernan & Yaqoob (2004); (3) Steenbrugge et al. (2005); (4) Gondoin et al. (2001); (5) Reeves et al. (2007); (6) Braito et al. (2007); (7) Wilms et al. (2001); (8) Fabian et al. (2002); (9) Vaughan & Fabian (2004); (10) Miller et al. (2008); (11) Ponti et al. (2006); (12) Uttley et al. (2004); (13) Pounds et al. (2004); (14) Iwasawa et al. (2004); (15) Nandra et al. (1999); (16) Turner et al. (2008); (17) Tombesi et al. (2007); (18) Reeves et al. (2004); (19) Markowitz et al. (2009); (20) Gondoin et al. (2003); (21) Ponti et al. (2009); (22) Page et al. (2003); (23) Pounds et al. (2003b); (24) Miller et al. (2007); (25) Vaughan et al. (2004); (26) Fabian et al. (2009); (27) Fabian et al. (2004); (28) Gallo et al. (2004); (29) Pounds et al. (2003a); (30) Pounds et al. (2009).

the broad Fe K_α line of 1800 eV, in agreement with the value found in the FERO analysis (1775^{+511}_{-594} eV). Fabian et al. (2004) proposed that the X-ray spectrum of this source is disc reflection dominated, and as the high value of the line *EW* implies, high element abundances were required, in a similar way to absorption-dominated models (Gallo et al. 2004). Recently, Fabian et al. (2009) have presented new timing-based arguments in favour of the relativistic nature of the broad features in this source with the simultaneous detection of broad Fe L and K lines[1]. However, Miller et al. (2010) has recently claimed that the Fabian et al. (2009) interpretation of the timing properties of the source is not unique and that solutions that do not invoke relativistic reprocessing might still be viable.

Figure 2 shows the ratios of the data to the continuum and data to the best-fit model in the 2–10 keV energy range for the sources with a relativistic 6.4 keV Fe K_α broad line detection. For MRK509, MRK766 and ARK120, the figures were produced with the model including the ionised continuum and 6.7 keV Fe K_α line. The latter set of plots indicates how well the baseline model used in this work describes the data. The deviation of the best-fit model and the data is limited below ∼10% in the whole 2–10 keV energy range used for fitting, and below ∼5% if one excludes the last energy bins (>8 keV) with poorer statistics. Despite the fact that by selection the sources in FERO are unobscured ($N_H < 2 \times 10^{22}$ cm^{-2}) for two sources, MCG-5-23-16 and IC4329A, a downturn in the ratio plot below 3 keV is noticeable and could indicate extra cold absorption, which in principle would not have been taken into account by our baseline model. However, for the particular case of these two sources, it is believed that this downturn cannot be attributed to extra cold absorption since the parameters derived from the warm absorption model (ABSORI) used yield values compatible with those extracted from CAIXA (as seen in Table C.1), N_H ($z = 0$) $(1.20^{+0.13}_{-0.02}) \times 10^{22}$ cm^{-2}, and $(0.33^{+0.04}_{-0.02}) \times 10^{22}$ cm^{-2} for MCG-5-23-16 and IC4329A, respectively, and in both cases, compatible with neutral absorption ($\xi < 0.02$ erg cm^{-1} s^{-1} for MCG-5-23-16 and $\xi < 0.47$ erg cm^{-1} s^{-1} for IC4329A). For these two sources, any extra neutral absorption that is present should have been taken into account by the model component ABSORI. Table 2 lists in the last column the χ^2 and corresponding number of degrees of freedom for those sources with evidence of a relativistic Fe K_α line.

4.2. Fraction of relativistic Fe lines

4.2.1. Detection fraction in FERO

The fraction of relativistic Fe lines detected in the FERO sample is 9% (13/149). Considering only the sources in the flux-limited sample, the detection fraction rises to 36% (11/31). These two numbers do not provide specific information on the *intrinsic* fraction of AGN that have broad Fe lines. They are limited by FERO being made of spectra of disparate quality and by the unavailability of a well-defined complete AGN sample. Nevertheless, the observed detection fraction can be considered as a lower limit for the intrinsic number of AGN that would show a broad Fe line if, for example, all sources were observed with the same signal-to-noise.

[1] We point out that the *XMM-Newton* spectra of 1H0707-495 included in the FERO sample correspond to the ones used by Fabian et al. (2004) and that Fabian et al. (2009) used a different dataset.

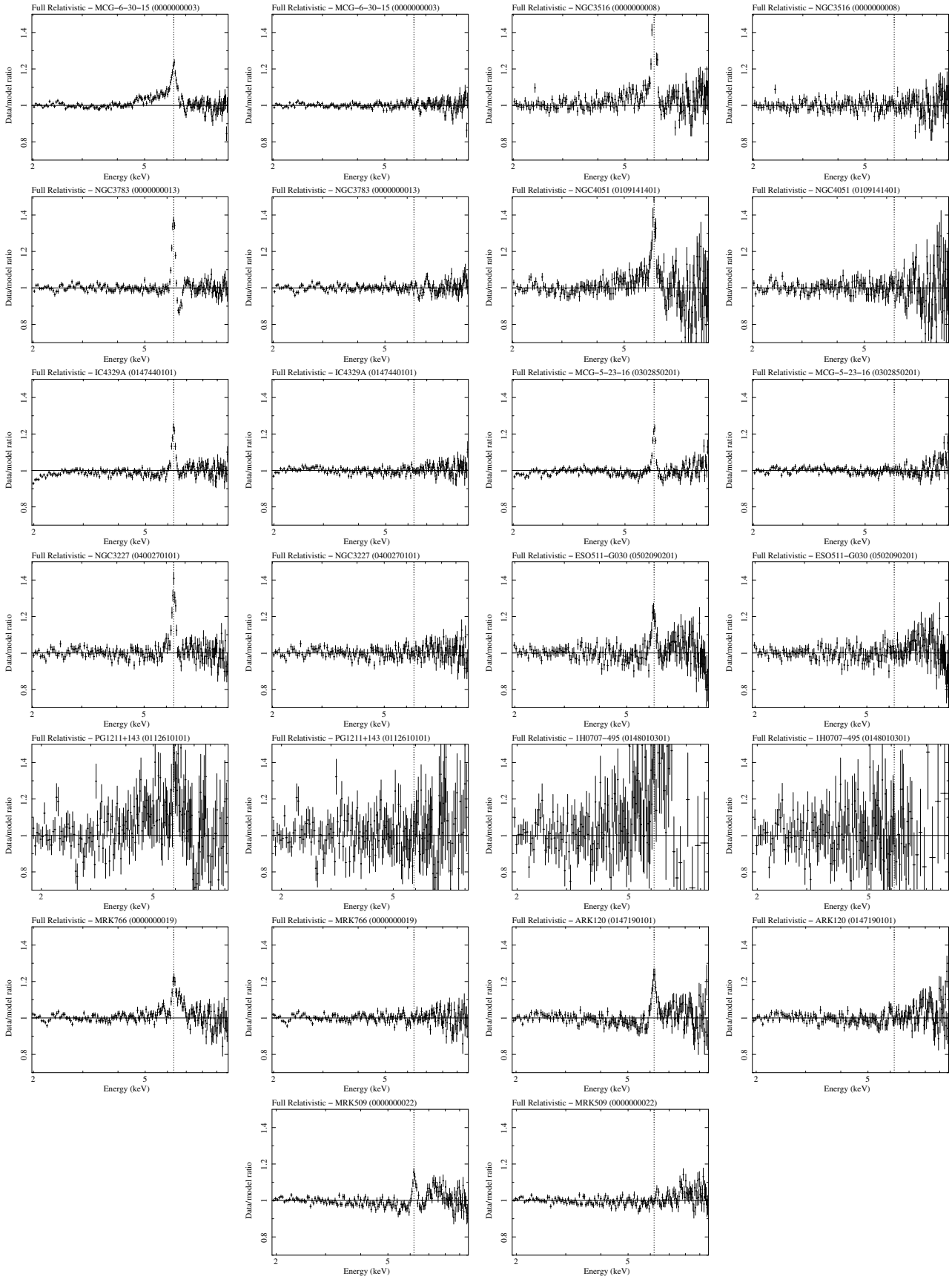

Fig. 2. Set of two figures for those sources with a relativistic 6.4 keV (6.7 keV) Fe K_α line *EW* detection $\geq 5\sigma$ confidence level: data to the best-fit continuum ratio (*left set column*), and data to the best-fit model ratio (*right set column*). The vertical dashed line is placed for reference at 6.4 keV (6.7 keV) in the rest frame of the source. On *top of each figure* the model used for the ratio, the corresponding source name, and the observation ID are given. For those sources with summed observations a *dummy* observation ID is given.

It is possible to estimate statistical errors on the detection fractions to reflect the uncertainty introduced by considering a limited number of sources. Detection fractions are calculated as val_1/val_2, where val_1 and val_2 indicate a given number of sources used to work out a given detection fraction. For the errors of $val_{1,2}$, Poisson statistics are assumed, where the errors are calculated as the average of the upper (Δ_{UL}) and lower limit (Δ_{LL}) of the 84% c.l. (which correspond to the commonly used $\Delta_{UL} = 1 + \sqrt{val_{1,2} + 0.75}$ and $\Delta_{LL} = \sqrt{val_{1,2} - 0.25}$, according to Gehrels 1986), both of which are good approximations for this moderate confidence level and are accurate to better than 5% even for low values of $val_{1,2}$ (see Gehrels 1986, for more information). The error of val_1/val_2 is propagated quadratically. In this way, the detections fractions and their associated errors are 9 ± 3% and 36 ± 14% for the FERO sample and for the flux-limited sample, respectively.

A broader understanding of the incidence of the relativistic line in our work can be achieved by considering the upper limits on the line intensity that characterize the majority of the sources. Within the FERO sample, ~16 ± 4% of broad line *EW* upper limits are below 100 eV. This value corresponds to the *EW* of a neutral disc with an inclination of 60°, for an illuminating power law of $\Gamma = 2$ and solar abundances (Matt et al. 1992). If the analysis is restricted to the 20 sources with no significant broad line within the flux-limited sample, the fraction of sources in which the line *EW* is limited below 100 eV is 50% (10/20) (for reference, for 75, 50 and 25 eV, the fractions are respectively 25%, 20%, and <13%). However, 5 sources within the flux-limited sample have measured *EW*s lower than and inconsistent with this threshold, implying deviations from the standard scenario either in terms of very high disc inclination (unlikely given the relatively unobscured nature of these AGN), element abundances lower than solar or a non-standard accretion disc geometry (George & Fabian 1991).

Last, Table D.1 in Appendix D lists the 20 sources with broad line upper limits in the flux-limited sample. In particular, four sources (MRK 279, NGC 5548, ESO 198-G24 and MRK 590) exhibit upper limits below 40 eV, arbitrarily chosen to be comparable to the lowest line *EW* detected. Explaining line *EW*s below this value in the framework of standard accretion theories is not straightforward, and it requires the use of non-standard system properties. Assuming the above threshold, the *non-detection fraction* of broad lines in the flux-limited sample can then be calculated as 13% (4/31). Otherwise stated, the presence of a broad line cannot be excluded a priori in the remaining 87% of the sources in the flux-limited sample (although the line is formally detected only in 36% of the sources at a 5σ level). This fraction is interpreted here as the upper limit to the fraction of AGN exhibiting relativistically broadened Fe lines in the parent population.

4.2.2. Detection fraction and warm absorber

In some cases, the use of the model component ABSORI could be regarded as too simplistic, however necessary for the approach considered here. Nevertheless, the influence of the selected warm absorption component for the baseline model in determining the detection fraction was tested by running a consistency check over the 31 sources belonging to the flux-limited sample. The test replaces the model component ABSORI by the more complex and complete ZXIPCF model and looks for a significant change in the fraction of detected broad lines and the average broad line *EW*. ZXIPCF uses a grid of XSTAR photoionised absorption models and allows defining a covering fraction, which has been fixed to 1, and column density and ionisation parameters of the absorbing material, which have been left free during the fitting procedure. The results of this test show that the introduction of the ZXIPCF model component does not significantly provide a better fit, and yield a detection fraction of broad iron K_α lines of 39 ± 15% (12/31). This result is fully consistent with the 36 ± 14% (11/31) derived when using ABSORI for the warm absorption, and concludes that the detection fraction is not significantly affected by the approach taken in this work to model the warm absorber. Out of the sources from the flux-limited sample listed in Table 2, only ESO511-G030 does not show evidence of a broad line at the 5 sigma level when using ZXIPCF. In turn, MRK704 and NGC4593 show a broad line at the 5.5σ and 5.3σ levels, respectively, both at the limit of our detection threshold of $5\,\sigma$. The average line *EW* derived from the detected lines is $\langle EW \rangle = 154 \pm 112$ eV ($\langle EW \rangle_w = 73 \pm 3$ eV), again both consistent with the results derived when using the absorption model ABSORI (see Sect. 4.3.1).

4.2.3. Detection fraction and X-ray luminosity

Eleven out of the 13 lines detected correspond to sources classified as Seyfert galaxies, while only 2 come from a source classified as quasar. In a similar manner to the previous section, this corresponds to a detection fraction of 13 ± 5% and ≤6% for Seyfert galaxies and quasars respectively. If the exercise is restricted to sources in the flux-limited sample, the detection fractions are 36 ± 15% and ≤92% for Seyfert galaxies and quasars, respectively. Owing to the low number of lines detected in quasars and the low number of quasars present in the flux-limited sample, only upper limits to the detection fraction can be derived.

Figure 3 shows the distribution of the 2-10 keV luminosity for the FERO sample, highlighting those sources for which a significant relativistic broad Fe K_α line detection has been found. All broad Fe line detections correspond to objects with luminosities below $\sim 10^{44}$ erg s^{-1}. To investigate a possible dependence of relativistic broadening on the source luminosity, the following three luminosity bins are defined: L1: $L_X < 0.25 \times 10^{44}$ erg s^{-1}; L2: $0.25 \times 10^{44} < L_X < 1.20 \times 10^{44}$ erg s^{-1}; L3: $L_X > 1.20 \times 10^{44}$ erg s^{-1}. Considering the FERO sample, each bin was chosen to contain the same number of sources (~50), with no further distinctions (see Table 3). No significant difference is found between the number of sources with a relativistic line when comparing the lowest luminosity bin L1 to the intermediate luminosity bin L2, either using the sources from the FERO (0.7σ) or flux-limited (0.5σ) sample. The highest luminosity bin L3 contains no detections. However, with the uncertainties in the detection fraction in the L3 luminosity bin (see Table 3), it is possible to estimate the difference in detection fraction between the L1 and L3 luminosity bins, at the 2.2σ and 0.9σ levels for the FERO and flux-limited samples, respectively. To remove the dependency with luminosity and check whether an intrinsic difference exist between Seyfert galaxies, and quasars in terms of detection fraction, a luminosity range containing the same number of Seyfert galaxies, and quasars is selected (L: $0.15 \times 10^{44} < L_X < 2.69 \times 10^{44}$ erg s^{-1}, Table 3). The detection fractions are 10 ± 7% (4/40) and ≤10% (2/40) for Seyfert galaxies and quasars, respectively, for sources in the FERO sample, and 18 ± 14% (3/17) and ≤92% (1/3) for sources in the flux-limited sample. The low number of detections prevents any statistically significant results from being drawn. Table 3 summarizes the different detection fraction for the different source

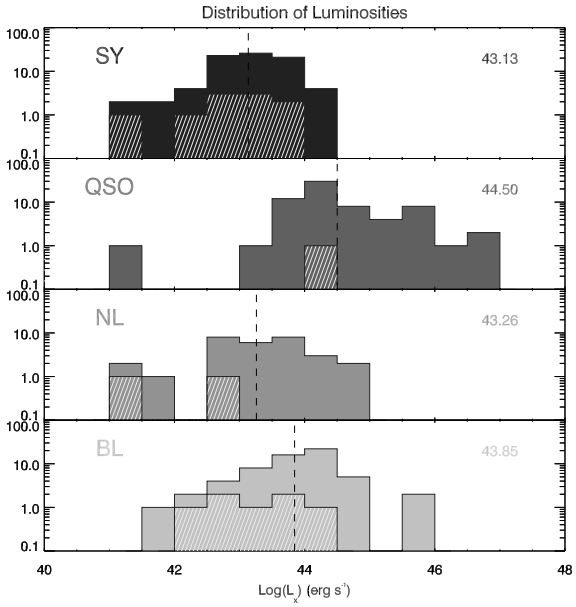

Fig. 3. X-ray luminosity distribution in the 2–10 keV energy band for the FERO sample. This sample has been split into Seyfert galaxies (Sy; 82 sources), quasars (QSO; 67 sources), narrow line (NL; 30 sources) and broad line (BL; 60 sources). The shaded area corresponds to the luminosity of those sources within the flux-limited sample for which a significant relativistic broad Fe K_α line detection has been found. The numbers shown on the right in each panel are the median values of the correspondent distribution, also marked by the vertical dashed line.

Table 3. Fraction of sources in the FERO sample with a significant relativistic broad Fe K_α line *EW* detection for different source type and luminosity class.

Obj. Class/ Luminosity	Sample	
	FERO (%)	Flux Limited (%)
Sy+QSO	9 ± 3 (13/149)	36 ± 14 (11/31)
Sy	13 ± 5 (11/82)	36 ± 15 (10/28)
QSO	≤6 (2/67)	≤92 (1/3)
NL	13±9 (4/30)	≤100 (2/4)
BL	12±6 (7/60)	35 ± 18 (7/20)
L1 (Sy+QSO)	16 ± 7 (8/50)	44 ± 22 (8/18)
L2 (Sy+QSO)	10 ± 6 (5/50)	27 ± 23 (3/11)
L3 (Sy+QSO)	≤2 (0/49)	≤47 (0/2)
L Sy	10 ± 7 (4/40)	18 ± 14 (3/17)
L QSO	≤10 (2/40)	≤92 (1/3)

Notes. Sy: Seyfert galaxy, QSO: quasar; NL: narrow line, BL: broad line; L1: $L_X < 0.25 \times 10^{44}$ erg s^{-1}; L2: $0.25 \times 10^{44} < L_X < 1.20 \times 10^{44}$ erg s^{-1}; L3: $L_X > 1.20 \times 10^{44}$ erg s^{-1}, where L1, L2 and L3 were chosen to contain the same number of sources (~50); L: $0.15 \times 10^{44} < L_X < 2.69 \times 10^{44}$ erg s^{-1}, L was chosen to contain the same number of Seyfert galaxy and quasars (40) (see text for details).

and luminosity class within the whole FERO and flux-limited samples. The correlation between the Fe K_α line *EW* and the hard X-ray luminosity based on individual source detections and within the flux-limited sample is investigated in Sect. 4.4. This analysis is extended to the remainder of the FERO sample in the companion paper by Longinotti et al.

Table 4. Weighted mean ($\langle EW \rangle_w$) and $1\sigma_w$ standard deviation, and mean ($\langle EW \rangle$) and 1σ standard deviation, of the Fe K_α line *EW* distribution.

Source Class	$\langle EW \rangle_w$	σ_w	$\langle EW \rangle$	σ
	(eV)	(eV)	(eV)	(eV)
SY+QSO (11)	76 ± 3	39	143 ± 27	91
SY (10)	72 ± 3	37	141 ± 30	95
QSO (1)	170 ± 22	–	170 ± 22	–

Notes. Only sources with an Fe K_α broad line detection within the flux-limited sample were used to compute these values. A distinction has been made according to source class. The number of sources used in each case to derive these values is in parenthesis).

4.3. Average properties of the relativistic broad Fe K_α line within the flux-limited sample

In the next two sections, the average properties of the relativistic broad Fe K_α line are discussed, first, in terms of the line equivalent width and second, in terms of the disc parameters derived from the *Kyrline* model. To derive meaningful results, only the 31 sources in the flux-limited sample are considered; therefore, information from the 11 sources (the first 11 sources listed in Table 2) with a broad Fe K_α line detection and the 20 sources with an upper limit of the broad Fe K_α line are used (see Table D.1).

4.3.1. Line equivalent width

For each source with a significant relativistic broad line detection, the measured value of the broad Fe K_α line *EW* is always below 300 eV (see Table 2). Considering all the detected lines, the mean value of the distribution of broad Fe K_α line *EW* is 143 ± 27 eV, with a 1σ standard deviation of 91 eV. It has to be kept in mind that the derived value for the mean is likely to overestimate the *true* mean of the distribution. The explanation can be found in the fact that the parent distribution of line *EW* is truncated by the ability to detect weak lines, which can only be found in sources with very a high signal-to-noise spectrum (see Fig. 1).

To derive a more representative value of the mean *EW*, the weighted mean of the Fe K_α broad line *EW* distribution was calculated using the 1σ statistical errors on the line *EW* for the individual weights. In this way, a weighted mean value of 76 ± 3 eV with 1σ standard deviation of 39 eV is obtained. This value is lower than the mean value derived above, and consistent with it to within ~1.3σ. There are two important caveats regarding the weighted mean. One, the calculation of the weighted mean assumes that the individual values of the line *EW* share the same underlying distribution and that such distribution is Gaussian, which does not necessarily have to be the case. Second, the use of the inverse square of the individual errors in the calculation of the weighted mean implies that, for a set of measurements with the same relative errors, the weighted mean is biased towards the lower values in the set. With a few exceptions, the relative errors in the line *EW* are comparable regardless of the value of the line *EW*, which implies that lower values of the line *EW* contribute more to the weighted mean. As a result, one could consider these two values, i.e. the mean and the weighted mean, one biased towards higher *EW* values and the other towards lower *EW* values, as the limits where the *true* mean of the distribution of relativistic broad Fe K_α line *EW* in AGN would be expected. Table 4 summarizes these results.

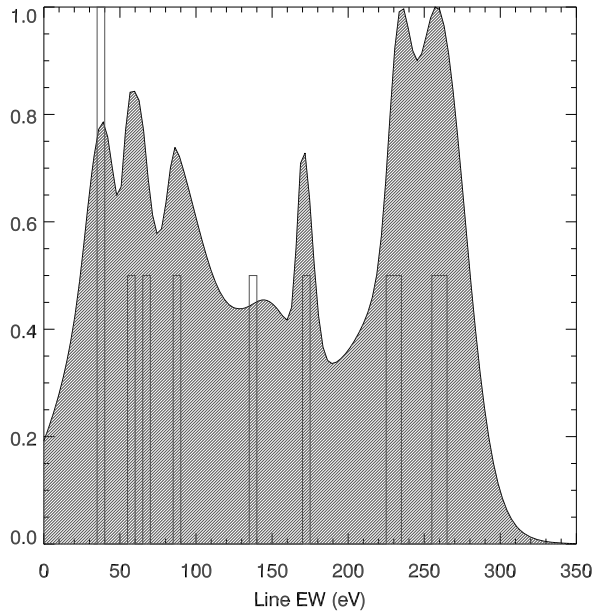

Fig. 4. Normalised distribution (shaded area) for the line *EW* for sources with a significant broad Fe K$_\alpha$ line detection within the flux-limited sample. The 1-dimensional histograms of this distribution is overlaid (white histogram).

Figure 4 shows the normalised distribution of the line *EW* for sources with a significant broad Fe K$_\alpha$ line detection within the flux-limited sample. This distribution is generated by combining one Gaussian distribution per measurement, where each Gaussian takes the mean and standard deviation of the corresponding best-fit-parameter value and its error at the 1σ level (upper or lower limits are not present in this plot). Overlaid on top of the Gaussian distribution is the corresponding 1-dimensional histogram, highlighting the contribution of each individual measurement to the overall distribution. Both distributions are normalised to their respective peak values.

4.3.2. Disc parameters

The *Kyrline* model parameters θ, β, and a respectively correspond to the disc inclination angle with respect to the observer, the power-law index of the radial disc emissivity law, and the black hole spin, and together they provide important information on the properties and conditions of the accretion disc. These values are reported in Table 2 for the sources with a significant broad Fe K$_\alpha$ line detection. For some sources, these parameters could not be constrained in the spectral fit and in these cases lower or upper limits are reported. Using only the parameters from the 11 line detections within the flux-limited sample, the mean and 1σ standard deviation values of θ, β and a are derived via the censored mean method described in Bianchi et al. (2009a). While these authors include measurements and upper limits, lower limits are also considered here. Table 5 lists these mean values and the 1σ standard deviation obtained using this method. (With only two spin measurements, the mean black hole spin is omitted.) Figure 5 shows normalised distributions for θ and β. As for the case of the distribution of the line *EW* in Sect. 4.3.1, these distributions are generated by combining one Gaussian distribution per measurement. The black hole spin is constrained well only in two cases, MCG-6-30-15 and MRK509, with a best-fit value of 0.86 ($^{+0.01}_{-0.02}$) and 0.78 ($^{+0.03}_{-0.04}$), respectively.

The mean value of β is about 2.4, but with a wide spread of values. Among the 11 sources, 6 have values of β higher than and

Table 5. Mean and 1σ standard deviation of the best-fit *Kyrline* model parameters for sources with a relativistic broad Fe K$_\alpha$ line detection.

Line Parameter (*Kyrline*)	Mean	σ
θ(°)	28 ± 1	5
β	2.4 ± 0.1	0.4

Notes. With only two spin measurements, the mean black hole spin is omitted.

inconsistent with 2, which means that emission is dominated by the innermost accretion disc regions. In three sources β is definitely lower than 2, and the emission is therefore dominated by the outermost regions. It must be recalled that a power law is often a poor approximation of the real emissivity law, which depends on the (unknown) geometry of the emitting corona. (See for instance Martocchia et al. 2000; Martocchia et al. 2002, for the emissivity laws in the *lamp-post* geometry.) It is, however, worth noting that in two sources, MCG-6-30-15 and MRK 509, β is about 4, or larger, which, under the *lamp-post* assumption, would imply an emitting source located at only a few gravitational radii from the black hole (Martocchia et al. 2002). In addition and for the case of MCG-6-30-15, Wilms et al. (2001) argue that this is not sufficient to explain the high β value and conclude that it is necessary to invoke magnetic extraction of the black hole spin energy to explain it (Blandford & Znajek 1977).

Not much can be said about the spin distribution. In five cases this parameter is totally unconstrained, since any permitted value of a is acceptable, and in another case it is rather poorly constrained ($a > 0.16$). In three cases, lower limits of about 0.5 can be placed, while in the remaining two sources, the measurements imply high values of the spin, but inconsistent with maximally rotating. It is interesting to note that, whenever a constraint can be placed, it always implies the rejection of the static black hole solution. However, this is a likely observational bias since non rotating black holes produce narrower lines, which are easier to detect with respect to the underlying continuum than lines produced by maximally spinning black holes, where the red tail of these lines can be confused with the underlying continuum. A maximally spinning black hole solution is statistically favoured than a static black hole solution. Given how few sources there are, the approximations made (see for instance the above discussions on β) and the subtle interplay between the various disc parameters, it is however premature to draw any firm conclusion in this respect.

The relation of the relativistic broad Fe K$_\alpha$ line intensity with θ, and β is also plotted in Fig. 6. As for black hole spin, constraints are too few (two sources only) to allow for discussion of any possible correlation of the line *EW* with a. These two distributions only show two things. First, the distribution of Fe K$_\alpha$ line intensity with θ is consistent with the fact that relativistic lines arising in accretion discs seen at high inclination angles rather than from face-on discs are more difficult to detect for a given value of the line *EW* (as noted by Nandra et al. 2007, see also Matt et al. 1992). Second, the apparent lack of detections of small *EW* lines with steep emissivity profiles is most likely an observational bias, and any real correlation between the two physical quantities can not be claimed.

4.4. Correlation studies within the flux-limited sample

Given all the upper limits derived for the line parameters, the censored fit approach was adopted. This procedure for linear

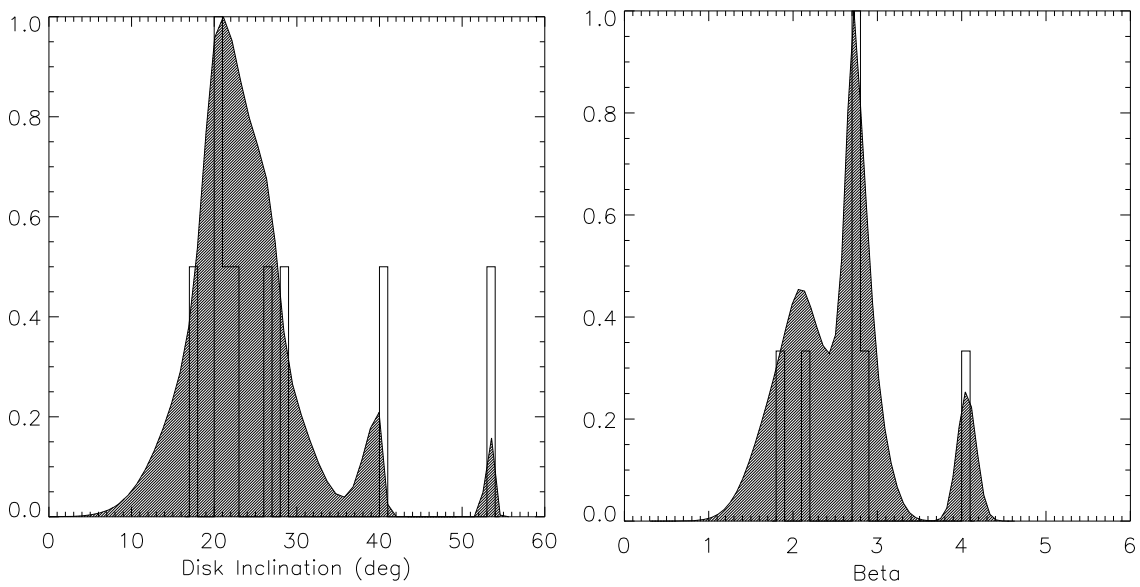

Fig. 5. Normalised distributions (shaded area) for the disc inclination angle (left) and disc emissivity (right) for sources with a significant broad Fe K_α line detection within the flux-limited sample. The 1-dimensional histograms of these distributions are overlaid (white histograms).

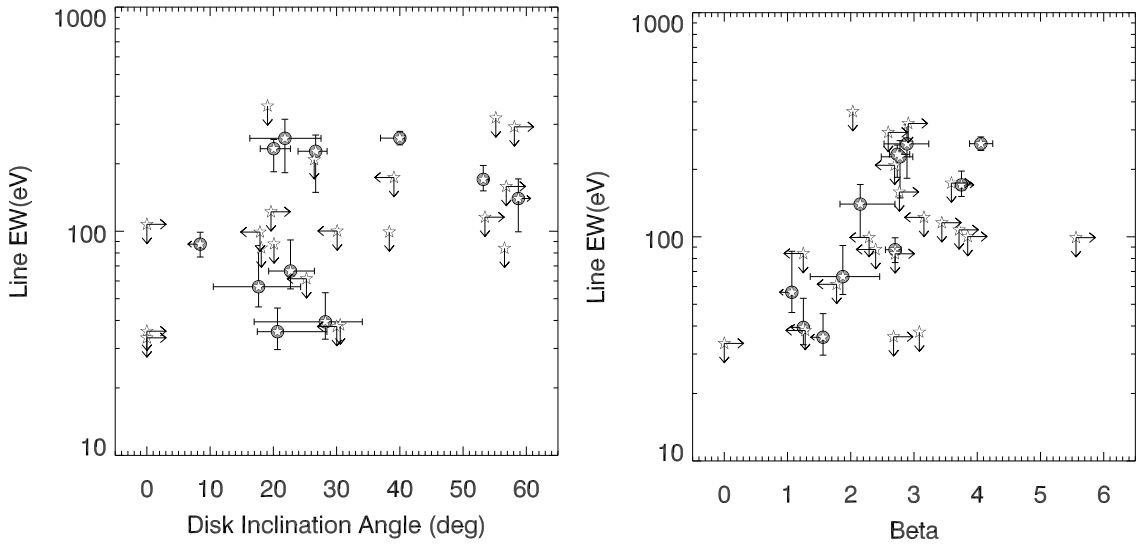

Fig. 6. Dependence of disc inclination angle and emissivity with the relativistic broad Fe K_α line *EW*. Filled circles indicate line detections at $\geq 5\sigma$ confidence level (where error bars indicate the 90% confidence level intervals), line upper limits are given at the 90% confidence level. *Kyrline* parameters upper and lower limits are given at the 90% confidence level.

fitting is applicable to data containing both measurements and upper and/or lower limits, and it is based on the method used by Schmitt (1985) and Isobe et al. (1986). Here it was applied in the same way as in Bianchi et al. (2009b). For each correlation analysis, the mean Spearman's rank correlation coefficient and null hypothesis probability were calculated. Only correlations with a null hypothesis probability lower than 10^{-3} (99.9% c.l.) will be considered statistically significant.

The correlations investigated in this work involve, on one hand, the broad Fe K_α line *EW* and the disc emissivity (β), and on the other, some source physical properties such as the black hole mass ($M_{\rm BH}$), the Eddington luminosity ($L_{\rm Edd}$), and the accretion rate (expressed in terms of $\frac{L_{\rm bol}}{L_{\rm Edd}}$). Within the censored fit method, the errors used for the line *EW* are 1σ errors, while the upper limits are at the 90% c.l.. In those correlations involving β, the censored fit approach described in Bianchi et al. (2009b) was slightly modified to account for the lower limits to the β parameter. The lower limit to β can be interpreted simply as consistent with 6 at the 90% c.l.. This value of 6 is the maximum value allowed for β in our model (see Sect. 3.3.1).

The values of the black hole mass were taken from the CAIXA catalogue (Bianchi et al. 2009a), and they are available for 24/31 of the objects in the flux-limited sample. (The reader is deferred to this paper for the references from which these values have been extracted.) Using the black hole mass ($M_{\rm BH}$), the Eddington luminosity was derived in this work according to the usual definition: $L_{\rm Edd} = (4\pi G M m_{\rm p} c) / \sigma_t = 1.26 \times 10^{38}$ $(M_{\rm BH}/M_\odot)$ erg s^{-1}. The accretion rate is considered as the ratio of the bolometric luminosity to the Eddington Luminosity: $\frac{L_{\rm bol}}{L_{\rm Edd}}$, where the bolometric luminosity has been derived by applying the following bolometric correction: $L_{\rm bol} = k_b \times L_{\rm x}$, where k_b is the correction factor dependent on the 2–10 keV X-ray luminosity (Lx) following Marconi et al. (2004). The hard X-ray luminosities derived in this work for those sources with a broad

Table 6. Source physical properties used in this work for those sources with a relativistic 6.4 keV Fe K_α line detection within the flux-limited sample.

Source name	$L_X^{2-10\ keV}$ (10^{44} erg s^{-1})	$Log_{10}(BH)$ ($M_\odot$)	L_{bol} (10^{44} erg s^{-1})	$L_{Eddington}$ (10^{44} erg s^{-1})	$L_{bol}/L_{Eddington}$
IC4329A	0.56	8.08	15.97	7.42	0.46
MCG-5-23-16	0.14	7.85	2.72	89.20	0.03
ESO511-G030	0.22	–	4.87	–	–
MCG-6-30-15	0.05	6.19	0.82	1.95	0.42
NGC4051	0.003	6.13	0.02	1.70	0.01
NGC3516	0.03	7.36	0.49	28.86	0.02
NGC3783	0.11	6.94	2.05	10.97	0.19
NGC3227	0.01	–	0.12	–	–
MRK509	1.04	7.86	35.37	91.28	0.39
MRK766	0.06	6.28	0.93	2.40	0.39
ARK120	0.90	8.27	29.58	234.6	0.13

Table 7. Results of the correlation studies within the flux-limited sample.

Broad Fe K_α Line EW (Y) vs.	a	b	Mean spearman rho	Null hypothesis probability
Black hole mass (X)	1.64 ± 0.12	-0.20 ± 0.11	-0.34	0.14
Accretion rate (X)	1.82 ± 0.15	0.08 ± 0.13	0.15	0.50
X-ray luminosity (X)	7.62 ± 5.16	-0.14 ± 0.12	-0.13	0.51
Beta (Y) vs.				
Black hole mass (X)	0.36 ± 0.11	-0.02 ± 0.09	0.05	0.75
Accretion rate (X)	0.38 ± 0.12	0.01 ± 0.10	0.12	0.59
X-ray luminosity (X)	-0.32 ± 4.19	0.01 ± 0.10	0.17	0.39

Notes. Mean intercept (a) and slope (b) for the linear fits of a log $(Y) = a + b \times \log(X)$ function described in the text. Errors in these two quantities are the statistical one standard deviation.

Fe K_α line detection are reported in Table 6, and they are in good agreement with those derived in the CAIXA catalogue.

Table 7 and Fig. 7 summarize the results of the correlation studies carried out. Table 7 lists the mean value of the Spearman's rank coefficient for the correlation of the broad Fe K_α line EW and β with the three physical parameters of interest, together with the corresponding null hypothesis probability. A negative value of Spearman rho indicates anti-correlation between the two parameters of interest. On the basis of these results, it is concluded that no statistically significant correlation is found with any of the considered physical properties of the AGNs.

Last, the relativistic Fe K_α line EW derived in this work and all the different parameters included in the CAIXA catalogue were correlated (see Table 1 in Bianchi et al. 2009a). No statistically significant correlation has been found with any of the parameters, including the $FWHM$ of the H_β line and the narrow Fe 6.4 keV K_α line EW. However, the low statistics prevents us from drawing any robust physical conclusions from the lack of such correlations.

5. Discussion

Despite the fact that the first relativistically distorted line in an AGN was observed about 15 years ago by ASCA (Tanaka et al. 1995; Nandra et al. 1997), and despite strong efforts to study them with more recent observatories, like *XMM-Newton* and *Suzaku*, there are still large uncertainties on the relative number of AGNs that possess such lines. The FERO project has been designed to address the fundamental question of how often these lines appear in AGN by estimating the fraction of objects where relativistic effects are detected on a well-defined sample. This number is crucial to establish if and how the standard AGN paradigm needs to be modified.

A collection of 149 radio-quiet Type 1 AGN, all targeted by *XMM-Newton*, has been assembled (the largest ever assembled for this kind of study) in order to tackle the question posed above. One fundamental requirement of the FERO project was to identify a complete and unbiased subsample of sources with high signal-to-noise spectra to be able to derive meaningful constraints on the physical properties of the sources. Only then it would be possible to extrapolate the results derived from this subsample to the unknown parent population of local radio-quiet AGN. A flux-limited sample of 31 objects was defined by selecting the XSS sources (see Sect. 2.2) with count rates in the 3–8 keV energy band greater than 1 cts/sec that fulfill the FERO selection criteria (i.e. local Type 1 radio-quiet X-ray unobscured sources). In this section the statistical properties of the flux-limited sample are discussed.

The baseline model used in FERO aims at providing the most accurate representation of the physical ingredients that are typically found in an average Type 1 AGN, so this model includes a Compton reflection component and absorption by line-of-sight ionised gas for modelling the continuum, a series of narrow Fe lines (5), and a relativistic Fe K_α line component fitted by the *Kyrline* model. The spin of the black hole, the radial emissivity profile of the accretion disc, and the disc inclination angle to the observer are free parameters in the fit of the line profile. To achieve a uniform analysis over the whole FERO sample, no attempt has been made to find the best-fit model on a source-by-source basis, nor has any attempt been made to find a best-fit model by using the FERO sample as a whole. To reduce the parameter space during the fitting procedure, several model parameters were investigated to see whether they could be constrained due either to physical, geometrical, or observational considerations. Tests were also carried out on including different model components in the baseline model, and the results have served either to consider them in the final baseline model or rule them

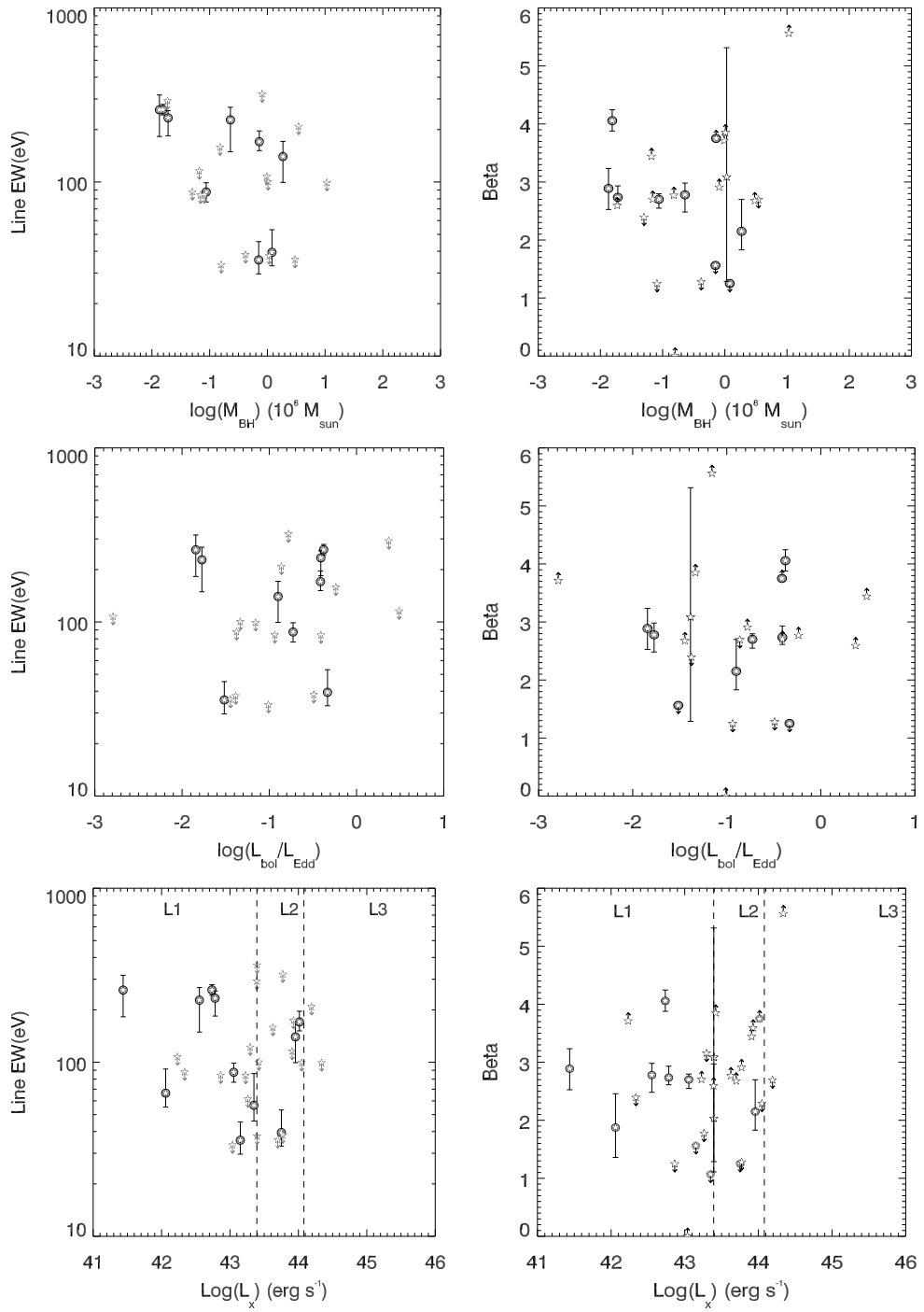

Fig. 7. From *top to bottom*, relativistic broad Fe K_α line equivalent width and β vs. black hole mass, accretion rate and hard X-ray luminosity. Filled circles indicate broad Fe K_α line detections at $\geq 5\sigma$ confidence level (where error bars indicate the 90% confidence level intervals). The dashed vertical lines in the bottom plots indicate the L1, L2, and L3 luminosity bins as described in the text (see Sect. 4.2.3).

out. The most important of these tests was the replacement in the baseline model of the neutral reflection component by an ionised reflection component, with the consequent change in the relativistic line from neutral iron to ionised iron. In fact, the results from these two scenarios were merged and presented as if coming from a single one.

Last, a consistency test was carried out by using the hard X-ray spectra of all the sources in the flux-limited sample, for which a significant detection of the relativistic line can be claimed (those listed in Table 2), by describing it with the most self-consistent reflection model envisaged, however keeping the model as simple as possible. The comparison of the results of this more complex and self-consistent model for the reflection components indicates that it does not significantly affect the results derived from the more phenomenological approach chosen for the baseline model adopted throughout the paper (refer to Appendix E for more details).

5.1. Fraction of relativistic lines

The main result of the FERO analysis is the relativistic broad line detection fraction, 36±14% in the flux-limited FERO subsample. The observed detection fraction is regarded as a lower limit to the intrinsic number of AGN that would show a broad Fe K_α

line if, for example, all sources were observed with the same, and sufficient, signal-to-noise ratio. It is important to stress once more that the observed detection fraction comes as a result of adopting a rather conservative detection threshold of 5σ confidence level, which is necessary since FERO does not focus on reporting individual broad line detections in particular objects. Instead, it focuses on statistical studies of the sample as a whole, which includes spectra of very different statistical quality. Nevertheless, as a reference, by relaxing this requirement to a 3σ confidence level, the above detection fraction rises to 61 ± 20% (19/31).

Upper limits on the line *EW* can also provide important information. For example, the fraction of sources in the flux-limited sample in which the broad Fe K_α line *EW* is limited below 100 eV is of the order of 50% (where 100% of line *EW* UL are below 360 eV). This result points to a much lower value of the average line intensity derived for local Type 1 AGN compared to the one derived from the mean spectra of high redshift ($z \gtrsim 1$) Type 1 AGN ($\langle EW \rangle \sim 560$ eV; Streblyanska et al. 2005), although there should be some caution in adopting this result since the high mean *EW* reported could come as a result of the method adopted for co-adding the spectra (Yaqoob 2006). The result derived in this work is also consistent with the upper limit of <400 eV derived by Corral et al. (2008). Using results on individual sources, the FERO analysis has provided upper limits below 40 eV in four sources (MRK 279, NGC 5548, ESO 198-G24, and MRK 590), which are constraining enough to have to stretch disc-accretion theories by requiring the use of non-standard system properties, such as very high disc inclination angles or element abundances significantly lower than solar (George & Fabian 1991).

The *non-detection fraction* of broad lines in the flux-limited sample is 13% (4/31). Inverting this argument, the presence of a broad K_α line cannot be excluded a priori in the remainder 87% (although the line is formally detected in 36% (11/31) of the sources). The value of 87% can be regarded as the upper limit to the intrinsic fraction of AGN where a relativistic Fe K_α line with $EW > 40$ eV could be present in the parent sample. Nandra et al. (2007) have fully explored the range of effects (geometry, ionisation, and element abundances) that would explain why a broad line is seen in some objects but not in others, so they are not repeated here.

A direct comparison of the results extracted from FERO with previous works reveals that the detection fraction of 36% derived for the flux-limited sample is consistent with previous results, such as those reported in Nandra et al. (2007) where a detection fraction of 35–40% was obtained. When compared to similar studies on sizable *XMM-Newton* samples (e.g. Nandra et al. 2007; Brenneman & Reynolds 2009), our sample differs in that our sample is very well-defined and homogeneously selected. Moderately X-ray obscured sources and radio-loud sources are both excluded from the FERO sample. However, the most significant differences are the model used to fit the relativistic profile, the fitting procedure, and the treatment of the sources with multiple observations. For instance, Brenneman & Reynolds (2009) fitted the continuum model on the entire *XMM-Newton* energy band, but they selected only one particular observation for each source, whereas Nandra et al. (2007) include multiple observations of the same target without combining them.

5.2. Disc parameters

The second goal of the FERO project was to derive average line and system properties and look into the question of whether a relativistic broad line can be associated to any source physical properties and, if so, investigate this dependence in more detail. The average broad line *EW* is of the order of 100 eV, however, a wide range of broad line *EW* (40–260 eV) are observed. As a reference, a neutral reflector covering half of the sky, as seen from the X-ray source ($\Omega/2\pi \sim 1$) and irradiated by a power-law spectrum with $\Gamma \sim 1.9$, should produce an Fe K_α line with equivalent width from around 100 to 150 eV in the inclination range 0°–60° and for solar abundances (George & Fabian 1991). Therefore, line *EW*s measured outside that range are likely to be produced mainly because i) the Fe abundance is different from solar, and/or ii) the reflector (disc) subtends a non-standard (smaller) solid angle as seen from the X-ray source. One physical scenario where broad line *EW*s $\gtrsim 150$ eV are plausible, involves reprocess emission from a photoionised accretion disc (Matt et al. 1993) or under a geometrical scenario which involves anisotropic emission.

The shape of the broad lines observed in the X-ray spectra of AGN are a potential carrier of information concerning the black hole spin. The issue of placing constraints to the black hole spin has been pursued by several authors (e.g. Nandra et al. 2007; Brenneman & Reynolds 2009). Using different approaches, both studies reached similar conclusions. While some objects show evidence of a spinning black hole, with the present data it is very difficult to reject the static solution. In this work the approach is that of modelling the line with a code capable of including the spin as a free parameter. The *Kyrline* model explicitly depends on the black hole spin. *Kyrline* is part of a suit of routines called KY (Dovčiak et al. 2004), a code that properly takes relativistic boosting, light bending, and time delays into account, assuming an axysymetric accretion disc geometry surrounding a black hole. As a general statement, the black hole spin is poorly constrained by the FERO analysis, except for MCG-6-30-15 ($0.86^{+0.01}_{-0.02}$) and MRK 509 ($0.78^{+0.03}_{-0.04}$) where the *Kerr* black hole solution is favoured. In five other sources, the static solution cannot be rejected, while in a further five, the constraint implies values of the black hole spin above ~0.5.

Another aspect of the present study is to try to establish the physical drivers behind the relativistic broad line by looking into any correlation between the presence and/or properties of the broad line *EW* and sources physical properties, such as black hole mass, X-ray luminosity, or Eddington ratio. However, using only sources from the flux-limited sample, no significant correlation has been observed between the broad Fe K_α line *EW* and these source properties. As previous works on large samples have done (e.g. Iwasawa & Taniguchi 1993; Bianchi et al. 2007; Corral et al. 2008), the FERO analysis has looked for inverse correlation between Fe K_α line emission and X-ray luminosity, the so-called IT effect (previously known a X-ray Baldwin effect), where the *EW* of the narrow Fe K_α emission line is inversely proportional to the 2–10 keV X-ray luminosity. Earlier results on a smaller sample (~100 AGN) using the spectra stacked residuals technique suggested that relativistic broad profiles follow a similar trend, where broad profiles are more common in low-luminosity AGN (Guainazzi et al. 2006). With information from individual source line profiles, the FERO analysis is unable to confirm such results, finding no statistically significant indication for the IT effect on broad Fe lines. However, it is worth pointing out that the lack of sources in the flux-limited sample with luminosities above 10^{44} erg s^{-1} prevents any firm conclusions. The IT effect will be investigated using the spectra stacked residuals technique using those sources in the FERO sample with an upper limit to the relativistic Fe K_α line *EW* (Longinotti et al., in prep.).

5.3. FERO in a wider context

An important remark should be made about the relativistic line in sources that are characterized by other phenomena. A recent paper by De Marco et al. (2009) carried out a systematic search for the presence of red- or blue-shifted components in the time-averaged spectra of the sources in the flux-limited sample. The study also looks into the spectral variability of these spectral components. A direct comparison with their results shows that 10 out of the 11 sources (~90%) within the flux-limited sample (all except ESO 511-G030) with a relativistic broad line indicate either red- or blue-shifted components, or both. In 6 out of these 10 sources (IC4329A, NGC 3783, NGC 3516, MRK 509, MCG-6-30-15, and MRK 766) there is evidence of significant variability (>90%) in the excess map (5.4–7.2 keV).

From the literature on the warm absorber phenomenon, we note that 9 out of 11 sources with line detections have warm absorbers: NGC 3783, NGC 3516, MRK 509, MCG-6-30-15, MRK 766, NGC 4051 (Blustin et al. 2005; McKernan et al. 2007), IC4329A (Steenbrugge et al. 2005), NGC 3227 (Markowitz et al. 2009). In the case of ESO 511-G030 the presence of line-of-sight ionised absorption has not been ascertained yet (Longinotti, private communication). The only 2 sources in the flux-limited sample with no warm absorber and no transient features are Ark 120 and MCG-5-23-16, so it is tempting to deem these two sources as the most robust detections, due to the lack of an alternative scenario to the relativistic line.

That sources with significant relativistic lines simultaneously show Fe *K* band variability and a warm absorber is probably twofold. There might be a physical connection between, e.g., the presence of the relativistic line and of the transient features, with some variability associated to it. But, it could well be the result of an observational bias, because these sources were extensively (and repeatedly) observed because they were known to be interesting a priori, so they ended up with the best signal-to-noise data and this explains the coincidence of the broad Fe line, warm absorber, and transient features in the same sources.

To conclude, it goes without saying that the FERO project would benefit from an expansion in several directions. The most obvious would be to complete the observations of the flux-limited sources such that the number of X-ray counts in the 2–10 keV fall above 1.5×10^5 cts. The expansion of the number of sources with 2–10 keV X-ray luminosities above 10^{44} erg s^{-1} would also allow studies like the IT effect to be carried out at a significant level and, of course, to investigate other correlations where the X-ray luminosity plays an important role.

Another crucial aspect to consider in future studies regarding relativistic disc lines is broadband coverage. This would allow exploration of the spectral regime above 10 keV and the opportunity to discern whether the spectral contribution at these energies can be attributed to a reflection component off distant matter and/or the accretion disc, analogous to the case of MCG-5-23-16 (Reeves et al. 2007). The importance of broadband coverage is also highlighted by, for example, the recent detection of a broad Fe K_α line in Fairall 9 in Suzaku observations, which have allowed a tight constraint on the black hole spin (Schmoll et al. 2009).

The FERO project has highlighted the importance of the availability of a complete and *well-exposed* AGN sample to shed some light on the origin and properties of the relativistic broad Fe lines in AGN, the environment, and conditions in which they are produced, and to provide better understanding of the scientific drivers needed for future high-throughput X-ray missions, such as IXO.

6. Conclusions

The main conclusions that are drawn from the results of the systematic and homogeneous spectral analysis of the large number of sources in FERO can be summarised as follows.

- The observed fraction of sources in the FERO sample that present strong evidence ($\geq 5\sigma$ significance) of a relativistic broad Fe K_α line is of the order of 9% (13/149). Considering only sources from the flux-limited sample, the detection fraction rises to around 36% (11/31). This number can be interpreted as a lower limit to the intrinsic fraction of AGN with relativistic Fe line broadening. The sources with a significant Fe K_α line detection mostly belong to sources with good statistical quality spectra ($\gtrsim 1.5\times10^5$ cts), so it is not surprising that the majority belong to the flux-limited sample. Considering only sources from the flux-limited sample, a broad Fe K_α line at the level of 40 eV can be rejected in 4 objects, 87%, which can be regarded as an upper limit to the intrinsic fraction of AGN with relativistic Fe K_α line broadening.
- There is no significant difference between Seyferts and quasars or narrow line and broad line objects in terms of detection fraction.
- All sources with a broad Fe K_α line detection have a hard X-ray luminosity in the 2–10 keV energy band below $\sim 1 \times 10^{44}$ erg s^{-1}. The difference in the detection fraction between the highest and lowest luminosity bins as defined in this work is only 2σ.
- From those sources with a significant Fe K_α line detection within the flux-limited sample, it is found that:
  - The average relativistic Fe K_α line *EW* is of the order of 100 eV (never higher than 300 eV for any given source).
  - The average system properties and 1σ standard deviation inferred from the *Kyrline* model can be summarised as:
    $\langle\theta\rangle = 28 \pm 5°$, consistent with an intrinsic random distribution of inclination angles.
    $\langle\beta\rangle = 2.4 \pm 0.4$, with a wide spread of values.
    The spin value a is poorly constrained, except for MCG-6-30-15 ($0.86(^{+0.01}_{-0.02})$) and MRK509 ($0.78(^{+0.03}_{-0.04})$) where the *Kerr* black hole solution is favoured.
  - No significant trend is found between the Fe K_α line *EW* and any of the line parameters investigated (θ, β, and a).
  - No significant correlation has been found between the Fe K_α line *EW* or disc emissivity (β) and the source physical properties investigated, such as, black hole mass, accretion rate, and hard X-ray luminosity.

Acknowledgements. This work is based on observations by *XMM-Newton*, an ESA science mission with instruments and contributions directly funded by ESA member states and NASA. I. de la Calle would like to acknowledge support by the Torres Quevedo fellowship from the Ministerio de Ciencia e Innovación Español and INSA. A.L. Longinotti acknowledges travel support provided by NASA through the Smithsonian Astrophysical Observatory (SAO) contract SV3-73016 to MIT for Support of the Chandra X-Ray Center, operated by SAO for and on behalf of NASA under contract NAS8-03060. We acknowledge financial support from the Faculty of the European space Astronomy Centre (ESAC). G. Miniutti thanks the Spanish Ministerio de Ciencia e Innovación Español and CSIC for support through a Ramón y Cajal contract. P.O. Petrucci acknowledges support by the PCHE (Phénomènes Cosmiques des Hauutes Energies) French working group. S. Bianchi, G. Matt and E. Piconcelli acknowledge financial support from Italian Space Agency, under grant ASI I/088/06/0. G. Ponti thanks ANR for support (ANR-06-JCJC-0047). We thank the referee for a careful reading of the manuscript and the useful comments that helped to improve it.

References

Anders, E., & Ebihara, M. 1982, Geochim. Cosmochim. Acta, 46, 2363
Antonucci, R. 1993, ARA&A, 31, 473
Arnaud, K. A. 1996, in Astronomical Data Analysis Software and Systems (ADASS) V, ASP Conf. Ser., 101, 17
Bianchi, S., & Matt, G. 2002, A&A, 387, 76
Bianchi, S., Matt, G., Balestra, I., Guainazzi, M., & Perola, G. C. 2004, A&A, 422, 65
Bianchi, S., Matt, G., Nicastro, F., Porquet, D., & Dubau, J. 2005, MNRAS, 357, 599
Bianchi, S., Guainazzi, M., Matt, G., & Fonseca Bonilla, N. 2007, A&A, 467, 19
Bianchi, S., La Franca, F., Matt, G., et al. 2008, MNRAS, 389, L52
Bianchi, S., Guainazzi, M., Matt, G., Fonseca Bonilla, N., & Ponti, G. 2009a, A&A, 495, 421
Bianchi, S., Fonseca Bonilla, N., Guainazzi, M, Matt, G., & Ponti G. 2009b, A&A, 501, 915
Blandford, R. D., & Znajek, R. L. 1977, MNRAS, 179, 433
Blustin, A. J., Page, M. J., Fuerst, S. V., Branduardi-Raymont, G., & Ashton, C. E. 2005, A&A, 431, 1111
Braito, V., Reeves, J. N., et al. 2007, ApJ, 670, 978
Brenneman, L. W., & Reynolds, C. S. 2009, ApJ, 702, 1367
Corral, A., Page, M. J., Carrera, F. J., et al. 2008, A&A, 492 ,71
Dadina, M. 2008, A&A, 485, 417
De Marco, B., Iwasawa, K., Cappi, M., et al. 2009, A&A, 507, 159
Done, C., Madejski, G. M., & ŻYcki P. T. 2000, ApJ, 536, 213
Dovčiak, M., Karas, V., & Yaqoob, T. 2004, ApJS.S., 153, 205
Fabian, A. C., & Miniutti, G. 2009, in Kerr Spacetime: Rotating Black Holes in General Relativity, eds. D. L. Wiltshire, M. Visser & S. M. Scott (Cambridge Univ. Press)
Fabian, A. C., Rees, M. J., Stella, L., & White, N. E. 1989, MNRAS, 238, 729
Fabian, A. C., Iwasawa, K., Reynolds, C. S., & Young A. J. 2000, PASP, 112, 1145
Fabian, A. C., Vaughan, S., Nandra, K., et al. 2002, MNRAS, 335, 1
Fabian, A. C., Miniutti, G., Gallo, L., et al. 2004, MNRAS, 353, 1071
Fabian A. C., Zoghbi, A., Ross, R. R., et al. 2009, Nature, 459, 540
Gabriel, C., et al. 2004, in Astronomical Data Analysis Software and Systems (ADASS) XIII, ASP Conf. Ser., 314, 759
Gallo, L. C., Tanaka, Y., Boller, Th., et al. 2004, MNRAS, 353, 1064
Gehrels, N. 1986, ApJ, 303, 336
George, I. M., & Fabian, A. C. 1991, MNRAS, 249, 352
Gondoin, P., Barr, D., Lumb, D., et al. 2001, A&A, 378, 806
Gondoin, P., Orr, A., Lumb, D., & Siddiqui, H. 2003, A&A, 397, 883
Guainazzi, M., Bianchi, S. & Dovčiak, M. 2006, Astron. Nachr., 10, 1032
Haardt, F., & Maraschi, L. 1992, ApJ, 413, 507
Isobe, T., Feigelson, E. D., & Nelson, P. I. 1986, ApJ, 306, 490
Iwasawa, K., & Taniguchi, Y. 1993, ApJ 413, L15
Iwasawa, K., Miniutti, G., & Fabian A. C. 2004, MNRAS, 355, 1073
Jansen, F., Lumb D., Altieri B., et al. 2001, A&A, 365, 1
Jiménez-Bailón, E., Piconcelli, E., Guainazzi, M., et al. 2005, A&A, 435, 449
Krongold, Y., Nicastro, F., Elvis, M., et al. 2007, ApJ, 659, 1022
Longinotti, A. L., Bianchi, S., Santos-Lleo, M., et al. 2007, A&A, 470, 73
Magdziarz, P., & Zdziarski, A. A. 1995, MNRAS, 273, 837
Marconi, A., Risaliti, G., Gilli, R., et al. 2004, MNRAS, 351, 169
Markowitz, A., Reeves J. N., Miniutti G., et al. 2008, PASJ, 60, 277
Markowitz, A., Reeves, J. N., George, I. M., et al. 2009, ApJ, 691, 922
Martocchia, A., Karas, V., & Matt, G. 2000, MNRAS, 312, 817
Martocchia, A., Matt, G., & Karas, V. 2002, A&A, 383, L23
Matt, G. 2002, MNRAS, 337, 147
Matt, G. 2006, AN, 327, 949
Matt, G., Perola, G. C., Piro, L., & Stella, L. 1992, A&A, 263, 453
Matt, G., Fabian, A. C., & Ross, R. R. 1993, MNRAS, 262, 179
McKernan, B., & Yaqoob, T. 2004, ApJ, 608, 157
Miller, L., Turner, T. J., Reeves, J. N., et al. 2007, A&A, 463, 131
Miller, L., Turner, T. J., & Reeves, J. N. 2008, A&A, 483, 437
Miller, L., Turner, T. J., Reeves, J. N., & Braito, V. 2010, MNRAS, 408, 1928
Miniutti, G., & Fabian, A. C. 2004, MNRAS, 349, 1435
Molendi, S., Bianchi, S., & Matt, G. 2003, MNRAS, 343, L1
Morrison, R., & McCammon, D. 1983, ApJ, 270, 119
Murphy, K. D., & Yaqoob, T. 2009, MNRAS, 397, 1549
Nandra, K., George, I. M., Mushotzky, R. F., Turner, T. J., & Yaqoob, T. 1997, ApJ, 477, 602
Nandra, K., George, I. M., Mushotzky, R. F., Turner, T. J., & Yaqoob, T. 1999, ApJ, 523, L17
Nandra, K., O'Neill, P. M., George, I. M., & Reeves, J. N. 2007, MNRAS, 382, 194
Osterbrock, D. E., & Pogge, R. W. 1987, ApJ, 323, 108
Page, M. J., Davis, S. W., & Salvi, N. J. 2003, MNRAS, 343, 1241
Panessa, F., Barcons, X., Bassani, L., et al. 2007, A&A, 467, 519
Piconcelli, E., Jimenez-Bailón, E., Guainazzi, M., et al. 2004, MNRAS, 351, 161
Piconcelli, E., Jimenez-Bailón, E., Guainazzi, M., et al. 2005, A&A, 432, 15
Ponti, G., Miniutti, G., Cappi, M., et al. 2006, MNRAS, 368, 903
Ponti, G., Cappi, M., Vignali, C., et al. 2009, MNRAS, 394, 1487
Porquet, D., Reeves, J. N., O'Brien, P., & Brinkmann, W. 2004, A&A, 422, 85
Pounds, K. A., Reeves, J., O'Brien, P., et al. 2001, ApJ, 559, 181
Pounds, K. A., Reeves, J. N., King, A. R., et al. 2003a, MNRAS, 345, 705
Pounds, K. A., Reeves, J. N., Page, K. L., Wynn, G. A., & O'Brien, P. T. 2003b, MNRAS, 342, 1147
Pounds, K. A., Reeves, J. N., King, A. R., & Page, K. L. 2004, MNRAS, 350, 10
Pounds, K. A., & Reeves, J. N. 2009, MNRAS, 397, 249
Puccetti, S., Fiore, F., Risaliti, G., et al. 2007, MNRAS, 377, 607
Read, A. M., & Ponman, T. J. 2003, A&A, 409, 395
Reeves, J. N., Turner, M. J. L., Pounds, K. A., et al. 2001, A&A, 365, L134
Reeves, J. N., Nandra K., George I. M., et al. 2004, ApJ, 602, 648
Reeves, J. N., Reeves, Awaki, H., Dewangan, G. C., et al. 2007, PASJ, 59, 301
Revnivtsev, M., Sazonov, S., Jahoda, K., & Gilfanov, M. 2004, A&A, 418, 927
Reynolds, C. S., & Nowak, M. B. 2003, Phys. Rev., 377, 389
Ross, R. R., & Fabian, A. C. 2005, MNRAS, 358, 211
Schmitt, J. H. M. M. 1985, ApJ, 293, 178
Schmoll, S., Miller, J. M., Volonteri, M., et al. 2009, ApJ, 703, 2171
Steenbrugge, K. C., Kaastra, J. S., Sako, M., et al. 2005, A&A, 432, 453
Stocke, J. T., Morris, S. L., Weymann, R. J., & Foltz, C. B. 1992, ApJ, 396, 487
Streblyanska, A., Hasinger, G., Finoguenov, A., et al. 2005, A&A, 432, 395
Strüder, L., Briel, U., Danner, K., et al. 2001, A&A, 365, 18
Tanaka, Y., Nandra, K., Fabian, A. C., et al. 1995, Nature, 375, 659
Terashima, Y., & Wilson, A. S. 2003, ApJ, 583, 145
Tombesi, F., de Marco, B., Iwasawa, K., et al. 2007, A&A, 467, 1057
Turner, T. J., & Miller, L. 2009, A&ARv, 17, 47
Turner, T. J., Reeves, J. N., Kraemer, S. B., & Miller, L. 2008, A&A, 483, 161
Uttley, P., Taylor, R. D., McHardy, I. M., et al. 2004, MNRAS, 347, 1345
Vaughan, S., & Fabian, A. C. 2004, MNRAS, 348, 1415
Vaughan, S., Fabian, A. C., Ballantyne, D. R., et al. 2004, MNRAS, 351, 193
Véron-Cetty, M. P., & Véron, P. 2006, A&A, 455, 773
Wilms, J., Reynolds, C. S., Begelman, M. C., et al. 2001, MNRAS, 328, 27
Yaqoob, T. 2006, in Conf. Proc. 230th Symp. IAU, Dublin (Ireland), ed. E. J. A. Meurs, & G. Fabbiano (Cambridge: Cambridge University Press), 461
Yaqoob, T., & Padmanabhan, U. 2004, ApJ, 604, 63
Yaqoob, T., George, I. M., Kallman, T. R., et al. 2003, ApJ, 596, 85

Pages 18 to 22 are available in the electronic edition of the journal at http://www.aanda.org

Appendix A: Sources from the flux-limited sample

List of 33 sources in the flux-limited sample. These sources have been selected from the RXTE all-sky Slew Survey (XSS, Revnivtsev et al. 2004) with a count rate in the 3–8 keV energy band greater than 1 cts/sec and fulfilling the FERO source selection criteria. The XSS is nearly 80% complete at the selected flux level for sources with Galactic latitude greater than 10°. For two of them, UGC 10683 and ESO 0141-G055, no *XMM-Newton* data were available as of April 2008. This leaves the number of XSS-selected bright sources in the FERO sample at 31.

Appendix B: List of sources with multiple observations that have not been summed

List of sources within the FERO sample where multiple observations are available but only one has been used (the one with longest exposure time).

Appendix C: Best-fit-model parameters for sources belonging to the flux-limited sample

Table C.1 gives some relevant best-fit-model parameters (see Sect. 3.3) for the 31 sources belonging to the flux-limited sample.

Appendix D: Relativistic Fe K_α line EW upper limits for the sources in the flux-limited sample

List of 20 sources within the flux-limited sample with an upper limit to the relativistic Fe K_α line *EW*.

Appendix E: A final self-consistent test on the detections within the flux-limited sample

As a final test, the hard X-ray spectra of all the sources in the flux-limited sample for which a significant detection of the relativistic line can be claimed has been described with the most self-consistent reflection model envisaged, but keeping the model as simple as possible. The baseline model comprises one layer of ionised absorption (the ZXIPCF model), reflection off cold distant matter including the most important emission lines and the associated self-consistent reflection continuum (the PEXMON model), and reflection from the accretion disc (the Ross & Fabian REFLION model, convolved with the KYRLINE kernel). Two ionised emission lines with energies fixed at 6.7 keV and 6.96 keV are also included as in the previous phenomenological models used throughout the paper, although they are not statistically required in all cases.

The PEXMON model is described in detail in Nandra et al. (2007) and describes the reflection spectrum from a cold slab of gas including both the reflection continuum and the most relevant emission lines, which are computed as self-consistently as possible according to the work by George & Fabian (1991). The metal abundances are fixed to the solar value (except for the case of MCG–6-30-15, see below) and the reflector inclination with respect to the line of sight to 60 degrees, which is appropriate for torus-like reflection in Seyfert 1 galaxies. The illuminating continuum is a power law with the same photon index as the power-law component of our spectral model. The REFLION model describes reflection off a ionised slab and is used instead to describe the disc reflection component. The illuminating photon index is the same as the primary continuum and the Fe abundance is fixed to the solar value (except for MCG–6-30-15, see below). The model is convolved with the kernel of the KYRLINE model (Dovčiak et al. 2004), which allows including all relativistic effects and measuring the relevant parameters.

It is important to stress once again that the goal here is not to provide the best possible fitting statistics but rather to compare the results of the phenomenological model used in the paper (which does not account for emission lines and associated reflection continua in a self-consistent manner) with a more physical spectral model. In some cases, more spectral components are included as explained in the subsequent section.

The results are reported in Table E.1, where the most important spectral parameters associated with the reflection components are considered. In Table E.2 the best-fitting relativistic parameters for both the phenomenological and the more physically motivated models are reported. Such a comparison implies that the more complex and self-consistent model for the reflection components does not significantly affect the results. Since the cases considered here correspond to the highest signal-to-noise data within the whole sample, the test supports the analysis carried out on the whole available sample within the context of the less sophisticated and more phenomenological model.

E.1. Notes on individual sources

Slight modifications to the baseline model described in Appendix E are given here for some individual sources. In the remaining cases, the baseline model was applied without being modified.

IC 4329A: absorption is best modelled with a neutral layer with moderate column density ($\simeq 4 \times 10^{21}$ cm^{-2}). A Gaussian absorption line with $EW \simeq -15$ eV was also included to model an absorption feature at ≃7.65 keV phenomenologically.

MCG-5-23-16: absorption is best modelled with a neutral layer with column density $N_H \simeq 1.5 \times 10^{22}$ cm^{-2}. The presence of a further ionised layer is possible but not statistically required.

MCG-6-30-15: the Fe abundance of the two reflectors was left free to vary in this case resulting in an overabundance of ∼× 3 with respect to the solar value. The model also comprises a Gaussian absorption line at ≃6.7 keV with $EW \simeq -15$ eV.

NGC 4051: a Gaussian absorption line with $EW \simeq -30$ eV was also included to model an absorption feature at ≃7.04 keV phenomenologically.

NGC 3516: a Gaussian absorption line with $EW \simeq -28$ eV was also included to model an absorption feature at ≃6.7 keV phenomenologically.

NGC 3783: a Gaussian absorption line with $EW \simeq -20$ eV was also included to model an absorption feature at ≃6.7 keV phenomenologically.

Mrk 509: a Gaussian absorption line with $EW \simeq -10$ eV was also included to model an absorption feature at ≃7.3 keV phenomenologically.

Table A.1. Flux-limited sample: 33 sources from the RXTE Slew Survey with a count rate in the 3–8 keV energy range greater than 1 cts/sec and fulfilling the FERO source selection criteria.

Source	Type	RXTE slew survey $(cts/s)_{3-8\ keV}$	*XMM-Newton* $(cts/s)_{2-10\ keV}$	*XMM-Newton* exposure time (ks)
NGC 4593	BLSY	1.05 ± 0.16	4.613 ± 0.009	53.2
MRK 704	BLSY	1.06 ± 0.22	0.984 ± 0.009	14.9
ESO511-G030	NCSY	1.10 ± 0.09	2.284 ± 0.005	76.2
NGC 7213	BLSY	1.12 ± 0.16	2.448 ± 0.009	29.6
AKN 564	NLSY	1.13 ± 0.02	2.246 ± 0.005	84.1
H1846-786	NCSY	1.15 ± 0.09	0.700 ± 0.011	6.3
MRK 110	NLSY	1.17 ± 0.10	3.362 ± 0.010	32.8
ESO198-G024	BLSY	1.21 ± 0.19	1.150 ± 0.003	85.3
FAIRALL9	BLQ	1.25 ± 0.02	1.313 ± 0.007	25.9
UGC 3973	BLSY	1.32 ± 0.12	1.304 ± 0.019	3.6
NGC 4051	NLSY	1.49 ± 0.02	2.783 ± 0.007	73.3
NGC 526A	NCSY	1.61 ± 0.14	2.177 ± 0.007	41.5
MCG-2-58-22	BLSY	1.61 ± 0.08	3.459 ± 0.021	7.2
NGC 7469	BLSY	1.69 ± 0.01	3.343 ± 0.005	142.6
MRK 766	NLSY	1.77 ± 0.12	1.962 ± 0.002	398.3
MRK 590	BLSY	1.95 ± 0.10	0.766 ± 0.003	72.0
IRAS05078+1626	NCSY	2.08 ± 0.19	2.691 ± 0.008	40.1
NGC 3227	BLSY	2.10 ± 0.02	3.635 ± 0.006	97.4
MR2251-178	BLQ	2.10 ± 0.11	2.387 ± 0.007	44.5
MRK 279	BLSY	2.13 ± 0.06	3.110 ± 0.006	104.8
ARK 120	BLSY	2.14 ± 0.03	4.553 ± 0.008	76.3
NGC 7314	NCSY	2.16 ± 0.04	4.509 ± 0.012	30.1
H0557-385	NCSY	2.33 ± 0.34	4.254 ± 0.021	10.5
MCG+8-11-11	BLSY	2.36 ± 0.27	4.838 ± 0.014	26.5
MCG-6-30-15	BLSY	3.08 ± 0.02	4.719 ± 0.004	295.1
MRK 509	BLQ	3.12 ± 0.10	4.432 ± 0.005	27.8
NGC 3516	BLSY	3.21 ± 0.01	1.841 ± 0.004	153.0
NGC 5548	BLSY	3.58 ± 0.02	4.191 ± 0.007	74.8
NGC 3783	BLSY	4.90 ± 0.04	5.539 ± 0.006	170.4
MCG-5-23-16	NCSY	6.46 ± 0.12	8.025 ± 0.008	110.3
IC 4329A	BLSY	7.29 ± 0.07	10.713 ± 0.011	85.1
UGC10683	SY	1.27 ± 0.18	–	–
ESO141-G055	SY	1.37 ± 0.12	–	–

Notes. These sources, with the exception of the last two sources, have all been the target of *XMM-Newton* observations. The *XMM-Newton* EPIC-pn count rate in the 2–10 keV energy range and exposure time is also given. For two of them, UGC 10683 and ESO 0141-G055, no *XMM-Newton* data were available as of April 2008. This reduces the number of XSS-selected bright sources in the FERO sample to 31.

Table B.1. List of sources within the FERO sample where multiple observations are available but only one has been used (the one with longest exposure time).

Source	List of *XMM-Newton* observation IDs combined	Date	Exposure (ks)
1H0707-495	**0148010301**	2002-10-13	70.0
	0110890201	2000-10-21	36.4
ESO113-G010	**0301890101**	2005-11-10	90.6
	0103861601	2001-05-03	4.0
ESO198-G24	**0305370101**	2006-02-04	85.3
	0067190101	2001-01-24	26.4
	0112910101	2000-12-01	6.8
IZW1	**0300470101**	2005-07-18	58.0
	0110890301	2002-06-22	18.4
MR2251-178	**0012940101**	2002-05-18	44.5
	0112910301	2000-11-29	3.5
MRK 841	**0205340201**	2005-01-16	30.1
	0112910201	2001-01-13	5.9
	0070740101	2001-01-13	7.6
	0070740301	2001-01-14	9.3
	0205340401	2005-07-17	17.3
NGC 2622	**0302260201**	2005-04-09	6.6
	0302260401	2005-10-08	4.5
NGC 4051	**0109141401**	2001-05-16	73.3
	0157560101	2002-11-22	46.2
NGC 4593	**0059830101**	2002-06-23	53.2
	0109970101	2000-07-02	8.8
PG 1211+143	**0112610101**	2001-06-15	49.5
	0208020101	2004-06-21	43.6
UGC 3973	**0400070201**	2006-09-30	14.5
	0103860801	2000-10-09	1.7
	0103862101	2001-04-26	3.6
PG 1116+215	**0201940101**	2004-12-17	69.3
	0201940201	2004-12-19	5.0
	0111290401	2001-12-02	5.5
IRASF12397+3333	**0202180201**	2005-06-20	68.7
	0202180301	2005-06-23	9.1

Notes. Observation IDs in bold correspond to those observations that have been considered, while observation IDs not in bold have been discarded.

Table C.1. Flux-limited sample: relevant best-fit-model parameters corresponding to the neutral reflection run and 6.4 keV relativistic Fe K$_\alpha$ line.

Source	Power Law	Warm Absorber		Compton Reflection		*EW* Narrow Fe K$_\alpha$ Emission Lines		
	Γ	N_H	ξ	R	Norm	Fe$_I$ 6.4 keV	Fe$_{XXV}$ 6.7 keV	Fe$_{XXVI}$ 6.96 keV
		(10^{22} cm^{-2})	(erg cm^{-1} s^{-1})		(10^{-3} keV^{-1} cm^{-2} s^{-1})	(eV)	(eV)	(eV)
AKN564	$2.82^{+0.05}_{-0.25}$	$0.76^{+0.17}_{-0.52}$	–	$2.22^{+0.62}_{-1.25}$	$18.38^{+1.36}_{-3.40}$	<18	13^{+10}_{-11}	<4
NGC526A	$1.52^{+0.10}_{-0.02}$	$1.24^{+0.42}_{-0.05}$	<0.47	<0.77	$4.46^{+0.49}_{-0.21}$	42^{+13}_{-17}	<26	<22
MCG-6-30-15	$2.05^{+0.02}_{-0.01}$	$0.80^{+0.04}_{-0.14}$	$6.30^{+1.97}_{-2.98}$	$0.51^{+0.29}_{-0.17}$	$17.38^{+0.23}_{-0.49}$	44^{+4}_{-4}	<5	<7
MRK766	$2.10^{+0.06}_{-0.05}$	$0.40^{+0.19}_{-0.12}$	$10.37^{+8.71}_{-4.92}$	$0.78^{+0.77}_{-0.42}$	>6.87	32^{+4}_{-6}	<21	20^{+9}_{-11}
NGC5548	$1.64^{+0.02}_{-0.01}$	<0.42	–	$0.20^{+2.82}_{-0.12}$	$8.57^{+0.46}_{-0.04}$	67^{+7}_{-12}	<4	<7
MCG+8-11-11	$1.78^{+0.05}_{-0.04}$	<6.24	–	$1.37^{+0.54}_{-0.48}$	$11.78^{+0.62}_{-0.56}$	97^{+10}_{-11}	<10	<17
MRK704	$1.72^{+0.04}_{-0.14}$	$9.67^{+3.82}_{-3.86}$	$105.42^{+74.83}_{-30.54}$	<3.33	$3.37^{+0.63}_{-0.84}$	<83	<42	<45
NGC3516	$1.61^{+0.06}_{-0.06}$	$4.48^{+0.63}_{-0.52}$	$77.03^{+11.98}_{-16.48}$	$1.99^{+0.22}_{-0.32}$	$4.02^{+0.14}_{-0.27}$	140^{+9}_{-13}	<7	<5
MCG-5-23-16	$1.65^{+0.04}_{-0.02}$	$1.20^{+0.13}_{-0.02}$	<0.02	$1.15^{+0.19}_{-0.18}$	$19.37^{+0.79}_{-0.48}$	32^{+6}_{-6}	<5	<5
NGC3227	$1.52^{+0.01}_{-0.02}$	$0.09^{+0.07}_{-0.03}$	<25.38	$0.15^{+0.12}_{-0.12}$	$6.70^{+0.09}_{-0.19}$	59^{+9}_{-18}	<5	8^{+6}_{-5}
H0557-385	$1.86^{+0.2}_{-0.05}$	$1.22^{+0.57}_{-0.32}$	$5.67^{+14.75}_{-5.24}$	<3.28	$13.63^{+4.12}_{-2.52}$	<31	<14	<26
NGC4593	$1.84^{+0.03}_{-0.04}$	<4.07	–	$1.24^{+0.32}_{-0.31}$	$11.88^{+0.44}_{-0.55}$	39^{+26}_{-16}	<10	14^{+8}_{-7}
NGC7469	>1.97	<0.53	–	$1.79^{+0.25}_{-0.19}$	$10.07^{+0.20}_{-0.07}$	73^{+5}_{-6}	<3	<9
NGC3783	$1.70^{+0.01}_{-0.01}$	$1.64^{+0.08}_{-0.06}$	$54.21^{+4.09}_{-4.70}$	$0.51^{+0.04}_{-0.43}$	$13.44^{+0.08}_{-0.17}$	90^{+3}_{-8}	<1	23^{+5}_{-3}
ESO511-G030	$1.93^{+0.02}_{-0.03}$	<1.38	–	$2.10^{+0.62}_{-0.10}$	$6.31^{+0.26}_{-0.06}$	11^{+0}_{-0}	<14	<12
IRAS05078+1626	$1.72^{+0.03}_{-0.06}$	$4.94^{+3.00}_{-4.05}$	–	$1.70^{+0.28}_{-0.76}$	$5.96^{+0.12}_{-0.38}$	38^{+21}_{-23}	11^{+10}_{-10}	<11
MRK279	$1.83^{+0.02}_{-0.03}$	<0.51	–	$1.16^{+0.10}_{-0.35}$	$7.79^{+0.07}_{-0.07}$	55^{+16}_{-14}	<3	7^{+7}_{-6}
MRK509	>1.96	<0.2	–	$2.49^{+0.07}_{-0.36}$	$12.88^{+0.10}_{-0.18}$	34^{+4}_{-4}	<4	<3
NGC7314	$2.09^{+0.11}_{-0.08}$	$1.35^{+0.32}_{-0.29}$	$4.86^{+5.88}_{-3.81}$	$1.16^{+1.00}_{-0.64}$	$18.22^{+2.45}_{-2.02}$	<56	14^{+10}_{-10}	27^{+11}_{-11}
NGC7213	$1.76^{+0.09}_{-0.02}$	<7.67	–	<0.77	$5.80^{+0.38}_{-0.30}$	82^{+14}_{-15}	22^{+13}_{-13}	17^{+13}_{-15}
IC4329A	$1.79^{+0.02}_{-0.01}$	$0.33^{+0.04}_{-0.02}$	<0.47	$0.93^{+0.07}_{-0.21}$	$26.85^{+0.18}_{-0.37}$	34^{+6}_{-9}	<4	8^{+4}_{-3}
MR2251-178	$1.32^{+0.03}_{-0.01}$	<0.61	–	$0.54^{+0.24}_{-0.48}$	$3.06^{+0.10}_{-0.04}$	23^{+11}_{-8}	<5	<2
H1846-786	$1.87^{+0.21}_{-0.10}$	<8.95	–	>0	$1.98^{+0.45}_{-0.19}$	78^{+60}_{-58}	<35	104^{+71}_{-72}
FAIRALL9	$1.90^{+0.05}_{-0.11}$	<2.67	–	$1.70^{+0.65}_{-1.05}$	$3.56^{+0.22}_{-0.28}$	107^{+27}_{-23}	<21	<29
UGC3973	$1.78^{+0.27}_{-0.16}$	<37.79	–	>0	$3.06^{+1.64}_{-0.59}$	156^{+57}_{-68}	<87	<38
MCG-2-58-22	$1.69^{+0.10}_{-0.04}$	<2.93	–	<3.32	$7.65^{+0.97}_{-0.49}$	<51	<20	21^{+27}_{-19}
NGC4051	$2.02^{+0.07}_{-0.01}$	$2.21^{+3.39}_{-0.64}$	–	<1.49	$9.48^{+1.09}_{-0.23}$	63^{+12}_{-13}	17^{+10}_{-11}	<17
MRK590	$1.61^{+0.08}_{-0.02}$	<3.39	–	$0.59^{+0.92}_{-0.39}$	$1.46^{+0.08}_{-0.04}$	113^{+16}_{-18}	<31	41^{+20}_{-15}
ARK120	$2.12^{+0.02}_{-0.03}$	<0.52	–	$2.14^{+0.35}_{-0.34}$	$15.95^{+0.31}_{-0.34}$	65^{+7}_{-7}	15^{+6}_{-6}	9^{+7}_{-7}
MRK110	$1.88^{+0.02}_{-0.06}$	<1.21	–	$1.47^{+0.25}_{-0.61}$	$8.58^{+0.12}_{-0.39}$	33^{+10}_{-10}	<6	<3
ESO198-G24	$1.79^{+0.07}_{-0.04}$	<2.57	–	$1.79^{+0.83}_{-0.51}$	$2.7^{+0.16}_{-0.09}$	60^{+12}_{-15}	<8	<8

Notes. Errors are given at the 90% confidence level. Upper limits to the relevant parameters are also given at the 90% confidence level. Sources with a significant broad Fe K$_\alpha$ line detection are marked in bold (as listed in Table 2).

Table D.1. Flux-limited sample: list of 20 sources with an upper limit to the relativistic Fe K$_\alpha$ line *EW*.

Source	Cts$^{2-10\ \mathrm{keV}}$ (10^5 cts)	*EW* upper limit (eV)
MRK 704	0.146 ± 0.012	362.1
FAIRALL9	0.341 ± 0.018	320.4
AKN 564	1.889 ± 0.043	292.3
MCG-2-58-22	0.250 ± 0.016	208.5
H1846-786	0.044 ± 0.007	173.7
MCG+8-11-11	1.284 ± 0.036	158.4
NGC 526A	0.903 ± 0.030	122.1
MRK 110	1.104 ± 0.033	115.6
NGC 7213	0.724 ± 0.027	107.4
UGC 3973	0.389 ± 0.020	100.2
H0557-385	0.446 ± 0.021	99.3
MR2251-178	1.062 ± 0.032	99.2
NGC 7314	1.358 ± 0.037	87.8
NGC 4593	2.455 ± 0.049	84.2
NGC 7469	4.769 ± 0.069	84.0
IRAS05078+1626	1.079 ± 0.033	61.4
MRK 279	3.259 ± 0.057	38.2
NGC 5548	3.133 ± 0.056	37.6
ESO198-G24	0.981 ± 0.031	35.8
MRK 590	0.552 ± 0.023	33.4

Notes. The *EW* upper limit is provided at the 90% confidence level.

Table E.1. Summary of the results of the self-consistent reflection model.

Source	Distant reflection	Disc reflection	Disc ionisation (erg cm s^{-1})	θ (°)	a	β	χ^2/d.o.f.
IC 4329A	0.5 ± 0.2	0.3 ± 0.2	150^{+80}_{-65}	34^{+11}_{-12}	≥0	$2.0^{+1.3}_{-0.9}$	197.2/163
MCG-5-23-16	0.3 ± 0.1	0.5 ± 0.3	≤70	31^{+7}_{-12}	≥0	$1.8^{+1.5}_{-0.8}$	247.3/164
ESO511-G030	0.7 ± 0.2	0.8 ± 0.4	70 ± 50	37^{+21}_{20}	≥0	$2.6^{+0.8}_{-1.7}$	185.0/162
MCG-6-30-15	0.2 ± 0.1	2.4 ± 0.8	62^{+40}_{-50}	39 ± 5	≥0.8	$3.4^{+0.8}_{-0.5}$	192.1/164
NGC 4051	0.9 ± 0.3	1.0 ± 0.5	140^{+90}_{-80}	18^{+9}_{-13}	≥0.3	$2.5^{+0.6}_{-0.5}$	172.0/162
NGC 3516	1.5 ± 0.3	1.8 ± 0.5	≤70	34^{+7}_{-12}	≥0.3	2.7±0.4	212.7/161
NGC 3783	0.8 ± 0.2	0.8 ± 0.4	≤90	27^{+19}_{-20}	≥0.2	$3.1^{+0.5}_{-0.4}$	221.4/163
NGC 3227	0.6 ± 0.2	0.5 ± 0.3	70^{+60}_{-60}	26 ± 9	≥0	$2.3^{+1.1}_{-0.7}$	226.5/162
MRK 509	0.3 ± 0.1	1.0 ± 0.6	80^{+40}_{-50}	≥45	≥0.4	$2.8^{+0.8}_{-0.5}$	244.2/160
MRK 766	0.3 ± 0.1	0.8 ± 0.4	700^{+120}_{-350}	28 ± 8	≥0.3	$2.6^{+0.4}_{-0.5}$	262.5/162
ARK 120	1.0 ± 0.3	0.7 ± 0.4	80^{+80}_{-30}	45 ± 10	≥0.1	$2.7^{+0.9}_{-1.2}$	188.7/160

Notes. All sources for which a detection of a relativistic line component is claimed in the paper have been described with two self-consistent reflection models, one for distant reflection (the PEXMON model), the other for disc reflection (the REFLION model). The relevant parameters and fitting statistics are reported in this table.

Table E.2. Comparison of the phenomenological and self-consistent model.

	Phenomenological model			Self-consistent model		
Source	θ (°)	a	β	θ (°)	a	β
IC4329A	28^{+6}_{-11}	≥0	≤1.3	34^{+11}_{-12}	≥0	$1.9^{+0.8}_{-1.0}$
MCG-5-23-16	21^{+8}_{-3}	≥0	≤1.6	31^{+7}_{-12}	≥0	$1.8^{+1.5}_{-0.8}$
ESO511-G030	18 ± 7	≥0	≤1.1	37^{+21}_{-20}	≥0	$2.6^{+0.8}_{-1.7}$
MCG-6-30-15	40^{+1}_{-3}	$0.86^{+0.01}_{-0.02}$	4.1±0.2	39 ± 5	≥0.8	$3.4^{+0.8}_{-0.5}$
NGC4051	22 ± 6	≥0.46	$2.9^{+0.3}_{-0.4}$	18^{+9}_{-13}	≥0.3	$2.5^{+0.6}_{-0.5}$
NGC3516	27^{+2}_{-3}	≥0.48	$2.8^{+0.2}_{-0.3}$	34^{+7}_{-12}	≥0.3	2.7±0.4
NGC3783	≤8	≥0.16	$2.7^{+0.1}_{-0.2}$	27^{+19}_{-20}	≥0.2	$3.1^{+0.5}_{-0.4}$
NGC3227	23 ± 4	≥0	$1.9^{+0.6}_{-0.5}$	26 ± 9	≥0	$2.3^{+1.1}_{-0.7}$
MRK509	53 ± 1	$0.78^{+0.03}_{-0.04}$	≥3.8	≥45	≥0.4	$2.8^{+0.8}_{-0.5}$
MRK766	20^{+3}_{-2}	≥0.47	$2.7^{+0.2}_{-0.1}$	28 ± 8	≥0.3	$2.6^{+0.4}_{-0.5}$
ARK120	≥59	≥0	$2.2^{+0.6}_{-0.3}$	48 ± 12	≥0.1	$2.7^{+0.9}_{-1.2}$

Notes. This table shows a comparison of the best-fitting relativistic parameters (only disc parameters are shown) obtained by applying the phenomenological model discussed throughout the paper (whose full results are given in Table 2) and the more self-consistent one discussed in Appendix E. Here, only sources for which a detection of a relativistic line component is claimed in the paper are shown.